Semiconductor Metal Oxides as Chemoresistive Sensors for Detecting Volatile Organic Compounds

Tingting Lin [1,2,*], Xin Lv [1,2], Zhineng Hu [1,2], Aoshu Xu [1,2] and Caihui Feng [1,2,*]

[1] College of Instrumentation and Electrical Engineering, Jilin University, Changchun 130061, China; xinlv15@mails.jlu.edu.cn (X.L.); huzn17@mails.jlu.edu.cn (Z.H.); xuks15@mails.jlu.edu.cn (A.X.)
[2] Key Laboratory of Geophysics Exploration Equipment, Ministry of Education of China, Changchun 130061, China
* Correspondence: ttlin@jlu.edu.cn (T.L.); jluhuihui@jlu.edu.cn (C.F.); Tel.: +86-135-0081-8835 (T.L.); +86-137-5694-8812 (C.F.)

Abstract: Volatile organic compounds (VOCs), which originate from painting, oil refining and vehicle exhaust emissions, are hazardous gases that have significant effects on air quality and human health. The detection of VOCs is of special importance to environmental safety. Among the various detection methods, chemoresistive semiconductor metal oxide gas sensors are considered to be the most promising technique due to their easy production, low cost and good portability. Sensitivity is an important parameter of gas sensors and is greatly affected by the microstructure, defects, catalyst, heterojunction and humidity. By adjusting the aforementioned factors, the sensitivity of gas sensors can be improved further. In this review, attention will be focused on how to improve the sensitivity of chemoresistive gas sensors towards certain common VOCs with respect to the five factors mentioned above.

Keywords: volatile organic compounds; semiconductor; metal oxide; gas sensor; sensitivity

1. Introduction

Volatile organic compounds (VOCs) are common in the environment and are encountered in many activities, such as painting a house, cooking, driving a car, oil refining and cutting the grass, etc. [1–3]. In other words, anthropogenic sources increase the release of VOCs beside natural sources. The increased emissions of VOCs have an adverse influence on the ambient air [4–8]. Moreover, certain volatile organic compounds are identified as hazardous gases and can cause severe diseases such as allergy, colon cancer, rectal cancer, and lung cancer [9]. Therefore, environmental monitoring is essential for evaluating the air quality [10–14].

Currently, effective analytical techniques, including gas chromatography and spectrometry, have been used to monitor VOCs [15,16]. Although these analytical techniques are sufficiently accurate, they are expensive, time-consuming and lack portability. Therefore, many researchers have attempted to design effective, cheap, fast response and small gas sensors for the quantification of VOCs. Based on the different sensing mechanisms, gas sensors are divided into several main types, including resistive, catalytic, optical and electrochemical [17]. Among them, resistive gas sensors based on semiconductor metal oxides have been considered attractive candidates for detecting hazardous VOCs due to the fast response and recovery time, ease of use, low-cost, high sensitivity and good portability [18–24].

Over the past decades, researchers have been working to improve the gas-sensing performance of semiconductor metal oxide gas sensors [25–33]. Sensitivity is one of the major parameters of semiconductor metal oxide gas sensors and is affected by many factors [34,35]. Although several reviews have been published on semiconductor metal oxide gas sensors, it is still necessary to

summarize the factors affecting the sensitivity for further improvement of the gas-sensing performance. Herein, we intend to provide a review on chemoresistive semiconductor metal oxide gas sensors for detecting VOCs, including ethanol, acetone, formaldehyde, toluene and acetylene. First, we introduce five different VOC gases and briefly describe the gas-sensing mechanism of chemoresistive semiconductor metal oxide gas sensors. Then, we summarize the five factors, including the microstructure, defect, catalyst, heterojunction and humidity that affect gas sensitivity. Finally, we review the recent developments in chemoresistive semiconductor metal oxide gas sensors towards five different kinds of VOCs.

2. Volatile Organic Compounds in the Environment

In general, organic compounds consist of at least one carbon and one hydrogen atom. On the basis of volatility, organic compounds are divided into three types: non-volatile organic compounds (NVOCs), semi-volatile organic compounds (SVOCs) and volatile organic compounds (VOCs) [33]. There are many definitions of VOCs according to different considerations. The U.S. Environmental Protection Agency (USEPA) defines VOCs as follows: "any carbon compounds excluding carbon monoxide, carbon dioxide, carbonic acid, metallic carbide, metallic carbonate and ammonium carbonate, which participate in atmospheric photochemical reactions" [29]. The World Health Organization (WHO) defines VOCs as: "organic compounds having the melting point below room temperature and the boiling point between 50–260 °C". However, China describes VOCs as "any organic chemical compounds that are easy to volatilize at normal pressure and temperature" [1].

Table 1 shows the chemical formula, formula weight, IDLH (immediately dangerous to life or health) concentration and TLV (threshold limit value) of VOCs. The TLV refers to the maximum concentration at which repeated exposure to VOCs can be endured without any adverse health effects [36,37].

Table 1. Chemical formula, formula weight, IDLH (immediately dangerous to life or health) and TLV (threshold limit value) of VOCs.

Gases	Chemical Formula	Formula Weight (g/mol)	IDLH (ppm)	TLV (ppm)
Ethanol	C_2H_5OH	46.07	3300	1000
Acetone	CH_3COCH_3	58.08	20,000	750
Formaldehyde	HCHO	30.03	20	0.75
Toluene	C_7H_8	92.14	500	100
Acetylene	C_2H_2	26.04	NA	NA

NA = not available.

2.1. Ethanol

Ethanol is a volatile, colourless transparent liquid with a melting point of −114 °C, and a boiling point of 78.3 °C. Ethanol is widely used in the fields of the defence industry, food industry, industrial and agricultural production as well as medical and health services. Ethanol has a particular smell, and can be used to make acetic acid [38], beverages [39] and essences [40]. In addition, ethanol is the raw material for producing dyes, paints and cosmetics. In the medical field, ethanol is also used as a medical disinfectant. Upon exposure to ethanol vapor, it may cause dizziness, headache, fatigue and nausea [41]. More importantly, ethanol vapor and air may form an explosive mixture, so it is necessary to monitor the concentration of ethanol in industrial production and road transportation practices.

2.2. Acetone

Acetone is a representative type of ketone. It is a clear and colourless liquid with a pungent odour. As a reagent, acetone is widely used as a diluting agent, cleaning agent and extraction agent in laboratories. Acetone is also used as an effective solvent in a range of industrial products, such as paints and agglomerants. The compound, which is one of the most essential raw materials for organic synthesis, is used to produce epoxy resins, polymethyl methacrylate and pharmaceutics.

Acetone can irritate the throat, nose and eyes [42,43]. Long-term exposure to acetone can result in pharyngitis, bronchitis and dermatitis. The quantitative detection of acetone is important for good health [44].

2.3. Formaldehyde

Formaldehyde has been widely used in many industries, such as the furniture, textile and printing industry [45]. It is a stimulating, colourless, pungent-smelling gas, easily soluble in water. Exposure to low levels of formaldehyde can lead to a variety of physical discomforts, such as dizziness, fatigue, chest distress, sore eyes, palpitation and nausea. Upon exposure to high levels of formaldehyde, the inhalation of gas can cause difficulty in breathing and lung oedema [46]. Due to the toxicity of formaldehyde, the Occupational Safety and Health Administration (OSHA) has established the TLV as a concentration of 0.75 ppm for 8 h. Indoor formaldehyde, which is emitted from antiseptics, glues, plastics, wood furniture and carpet cleaners, is closely related to people's daily life [47]. For environmental and safety purposes, manufacturing gas sensors for formaldehyde detection is urgent.

2.4. Toluene

Toluene is a clear, colourless volatile liquid with a particular aromatic odour, and is insoluble in water, but soluble in ethanol and acetone [48]. Toluene is one of the most widely used aromatic hydrocarbons and has many applications in the manufacture of adhesives, dyes, medicine, pesticides, rubber, fingernail polish and explosive materials [49]. In urban areas, toluene is emitted in processes related to automobile exhaust and gasoline. Moreover, toluene is an irritant to the skin and the mucous membrane. At higher concentrations, toluene can cause nervousness, restlessness and a rapid heartbeat. Toluene may also cause damage to the liver or kidneys. The OSHA has defined the permissible exposure limit for toluene as 100 ppm for 8 h [50]. Toluene is considered a kind of cancer biomarker. In fact, high levels of toluene can be detected in the exhaled breath of people with lung cancer compared to healthy non-smokers. Hence, the development of a high performance toluene sensor is not only of medical but also of social importance.

2.5. Acetylene

Acetylene is a reactive and unstable hydrocarbon gas [51]. It is a raw material of acetaldehyde, acetic acid, benzene, synthetic rubber, paints, dry-cleaning solvents and insecticide sprays [52]. In addition, the combustion of the compound is used for illumination, cutting metals and oxyacetylene welding [53]. However, acetylene can be explosive in the pressurized form and in the presence of electric sparks. Acetylene has a weak narcotic effect and prevents cell oxygenation. Upon exposure to high levels of acetylene, oxygen in the air is forced out, resulting in suffocation.

3. Gas-Sensing Mechanism of Semiconductor Metal Oxide Sensors towards Volatile Organic Compounds

To fabricate high performance sensors that are used for monitoring VOCs, it is necessary to understand the gas-sensing mechanism. In general, a gas sensor based on semiconductor metal oxides can be applied to detecting the target gas via a redox reaction between the gas molecules and the sensing material [54]. In the presence of air, oxygen gas is absorbed on the surface of the sensing material, resulting in adsorbed oxygen. Due to different working temperatures, adsorbed oxygen are different oxygen species including O_2^-, O^- and O^{2-} [55]. The adsorption kinematics are described as the follows:

$$O_2(\text{gas}) \rightarrow O_2(\text{absorbed}) \tag{1}$$

$$O_2(\text{absorbed}) + e^- \rightarrow O_2^- \tag{2}$$

$$O_2^- + e^- \rightarrow 2O^- \tag{3}$$

$$O^- + e^- \rightarrow O^{2-} \tag{4}$$

The formation of oxygen species results in the capture of electrons from the conduction band, leading to a change in conductivity of the semiconductor metal oxide [56]. The variation in conductivity results from a change in the charge carrier concentration. According to the different types of major carriers, semiconductor metal oxide is classified into n-type and p-type. The charge carriers of n-type semiconductor metal oxide are electrons, so the interaction between the semiconductor metal oxide and the ionic oxygen species causes a decrease in conductivity upon exposure to air. In contrast, the charge carriers of p-type semiconductor metal oxide are holes, resulting in an increase in conductivity [57].

The well-accepted gas-sensing mechanism is described as a change in conductivity of the sensor [58−60]. Herein, a brief introduction to the sensing mechanism of n-type semiconductor metal oxide is given based on the example of SnO_2, as shown in Figure 1 [61]. In air, the oxygen molecules are adsorbed on the surface of semiconductor metal oxide, forming a potential barrier. The interaction between oxygen molecules and semiconductor metal oxide forms charged oxygen species by capturing electrons from the conduction band, leading to an electron-depleted region and band bending on the surface of the semiconductor metal oxide. The electron-depleted region is also referred to as the space-charge layer, as shown in Figure 1a. Its thickness is the length of the band bending region. The variation in band bending increases the resistance of the sensor. When the sensor is exposed to HCHO, HCHO will react with the adsorbed oxygen ions and release the trapped electrons back to the semiconductor metal oxide, resulting in an increase in the carrier concentration. As a consequence, the thickness of the space-charge layer is reduced, resulting in a decrease of the potential barrier and resistance, as shown in Figure 1b.
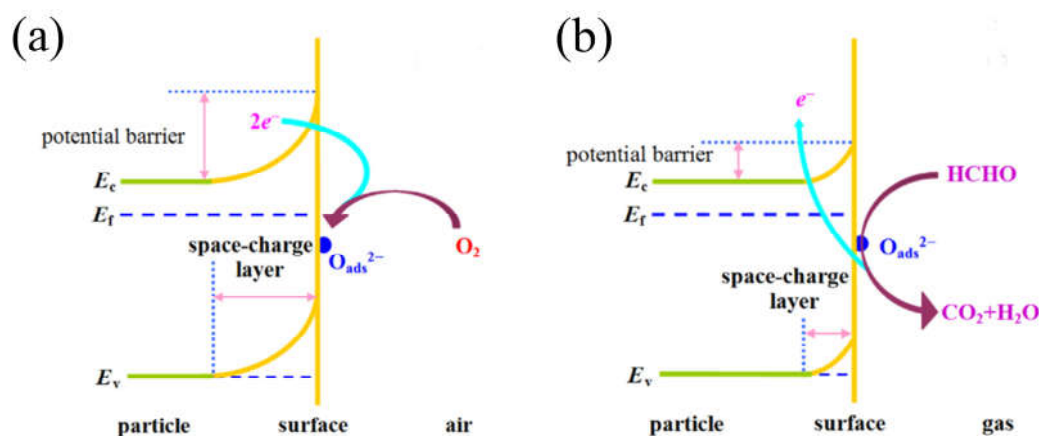

Figure 1. A schematic diagram of reaction mechanism of SnO_2-based sensor to HCHO: (**a**) in air, (**b**) in VOC. Reprinted from [61] with permission.

4. Factors Affecting the Sensitivity of Semiconductor Metal Oxide Gas Sensors

Sensitivity is a parameter reflecting the resistance variation in a certain concentration of target gas. For n-type semiconductor metal oxide sensors, the sensitivity is defined as R_g/R_a for oxidizing gases and R_a/R_g for reducing gases, where R_a and R_g are the resistances of the gas sensors in the presence of air and target gases, respectively. However, the sensitivity of p-type semiconductor metal oxide sensors has the opposite definition. The enhancement of sensitivity is of great importance in obtaining excellent gas sensors. Researchers have devoted great efforts to fabricate

high performance gas sensors [62–71]. The sensitivity of semiconductor metal oxide gas sensors can be improved by adjusting the microstructure, defects, catalyst, heterojunction and humidity.

4.1. Effect of the Microstructure

The response of semiconductor metal oxide sensors is based on the interaction between the target gases and adsorbed oxygen species. The adsorption-diffusion-desorption process occurs on the surface of the semiconductor metal oxide sensor. Therefore, the gas-sensing performance is influenced by the morphology of the semiconductor metal oxide. The optimal morphology promotes the adsorption and desorption of the adsorbed oxygen species, which plays a crucial role in the enhancement of the gas-sensing performance. Thus, it is necessary to understand the parameters of the microstructure for further improvement of gas sensors [25]. The grain size, number of activated adsorption sites and gas diffusion ability are the structural parameters that dramatically affect the gas-sensing performance.

4.1.1. Grain Size

The reduction in grain size to the nanoscale is one of the most effective strategies for the enhancement of the gas-sensing properties. In other words, the sensitivity of a gas sensor is directly affected by the grain size [72]. To gain insight into the impact of the grain size on sensitivity, Xu et al. proposed a model to illustrate the remarkable grain size effect [73]. As shown in Figure 2, the sensing material was composed of partially sintered grains connected to each other by necks [28].
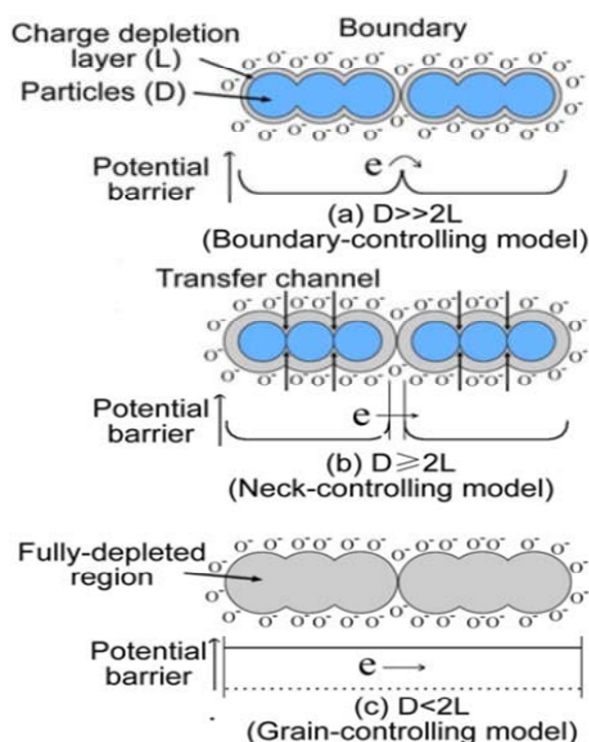

Figure 2. Schematic model of the effect of the crystallite size on the sensitivity of semiconductor metal oxide gas sensors: (**a**) D >> 2 L; (**b**) D ≥ 2 L; (**c**) D < 2 L. Reprinted from [28] with permission.

The interconnected grains formed larger aggregates connected to each other by the grain boundaries. Generally, there are three cases with respect to the relationships between the grain size (D) and the width of the space-charge layer (L), which are described in terms of the boundary control, neck control and grain control. For large enough grains (D >> 2 L), most grains were unaffected by the surface interactions with the gas phase. The predominant impact of gas on the conductivity of the sensor was provided by the grain boundary barriers, as shown in Figure 2a. Therefore, the grain boundary controlled the gas-sensing mechanism. The sensitivity of the sensing

material was independent of the grain size. For grains with D ≥ 2 L, the space-charge layer around each neck formed a conduction channel, as depicted in Figure 2b. The conductivity could be decided collaboratively by the cross-sectional area of those channels and the grain boundary barriers, resulting in an enhanced sensitivity. Furthermore, the sensitivity of the sensing material became dependent in the grain size and increased with the reduction in the grain size. For grains with D < 2 L, the space-charge layer extended throughout the whole grains. As seen from Figure 2c, the grains were almost fully depleted of mobile charge carriers. The conduction channels between the grains were mislaid, leading to a dramatically decreased conductivity. Due to the lack of significant barriers for the interconnected grain charge transport, the energy bands were nearly flat throughout the grains. Clearly, the sensitivity of the sensing material was controlled by the grains. It was found that the highest sensitivity was achieved in the case of D < 2 L. Based on Xu's model, Liang et al. have prepared highly monodisperse α-Fe$_2$O$_3$ nanoparticles with an average particle size of 3.1 nm, which exhibited an excellent acetone sensing performance due to the relation between the grain size (D) and the width of the space-charge layer (L) according to D < 2 L [74]. The almost fully depleted grains induced changes to the overall conductivity, leading to improvement of the sensitivity.

4.1.2. Number of Activated Adsorption Sites

It is well acknowledged that the sensing reaction of a gas sensor occurs at the active sites on the semiconductor metal oxide surface. Therefore, the number of activated adsorption sites has a great influence on the improvement of the gas-sensing performance. One good strategy to increase the number of active sites is the adoption of increased the specific surface area, which has a potentially strong impact on the adsorption ability of gas sensors. Accordingly, many researchers have strived to increase the specific surface area for obtaining enhancement of the sensitivity. For example, Zhang et al. synthesized Co$_3$O$_4$ products based on the core-shell (CS) nanostructure, porous core-shell (PCS) nanostructure, porous popcorn (PPC) nanostructure, and nanoparticle (NP) nanostructure to verify that the specific surface area affected the sensitivity of gas sensors [75]. As shown in Figure 3a, the specific surface areas of CS-, PCS-, PPC-, and NP-Co$_3$O$_4$ were 44.5, 42.8, 42.4 and 12.2 m^2·g^{-1}, respectively. The response values of CS-, PCS-, PPC-, and NP-Co$_3$O$_4$ towards 200 ppm acetone were 13, 11, 7.9, and 2.6, respectively (Figure 3b). Obviously, the larger specific surface endowed the Co$_3$O$_4$ nanostructures with more activated adsorption sites, thereby increasing the adsorption of gas molecules and improving the sensitivity of the gas sensor.
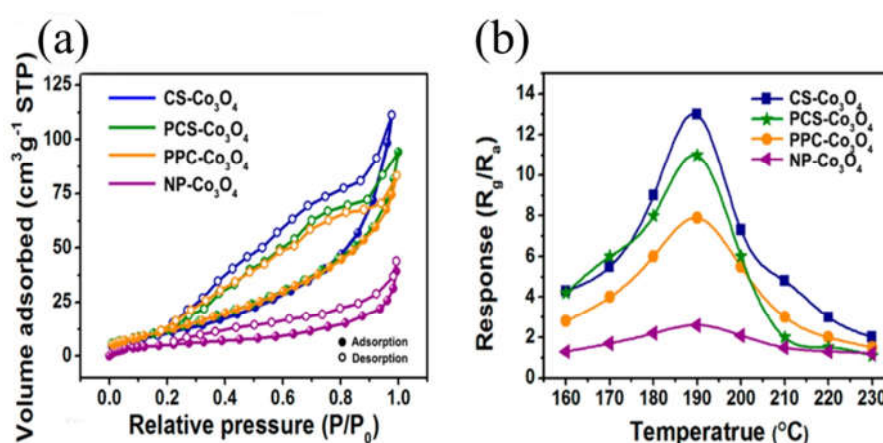

Figure 3. (**a**) N$_2$ adsorption-desorption isotherms of Metal-Organic Frameworks-derived Co$_3$O$_4$ structures; (**b**) Responses of CS-, PCS-, PPC-, and NP-Co$_3$O$_4$-based sensors at different operating temperature toward 200 ppm acetone; Reprinted from [75] with permission.

4.1.3. Gas Diffusion

Except for the large specific surface area, enhancing the gas diffusion of the sensing materials is one strategy that can improve the gas-sensing performance. Generally, the sensing materials of gas sensors are classified into dense and porous nanostructures. In the case of dense nanostructures, gas diffusion can only occur on the surfaces of sensing materials because the gas molecules cannot penetrate into the sensing materials. In the case of porous nanostructures, the gas molecules can interact with the inner grains because the special structures are conducive to the penetration of gas molecules into the sensing materials. Sufficient diffusion can lead to a large change in the resistance of the gas sensor. The porous structure is divided into microporous, mesoporous and macroporous structure based on the pore size. The pore size of a microporous structure is smaller than 2 nm, whereas the pore size of a mesoporous structure ranges from 2–100 nm. The macroporous structure has a pore width larger than 100 nm. The porosity of semiconductor metal oxide has a profound effect on the gas diffusion depth, thereby affecting the sensitivity of the gas sensor. Sakai et al. proposed a theory of gas diffusion controlled sensitivity [76]. The diffusion of mesoporous nanostructures could be described by the Knudsen diffusion. The Knudsen diffusion coefficient (D_k) is related to the pore width (r), temperature (T) and molecular weight (M) of gas molecule:

$$D_k = \frac{4r}{3}\sqrt{\frac{2RT}{\pi M}} \tag{5}$$

The response of mesoporous nanostructures varied directly with the Knudsen diffusion coefficient (D_k) and inversely with the thickness (L) of the sensing film. Notably, the gas diffusion increased with increasing pore radius, contributing to an increase in the sensor response. In addition to Knudsen diffusion, there was another type of gas diffusion as the pore size was larger than 100 nm. The alternative type of gas diffusion allowed gases to diffuse more quickly through molecular diffusion, which is analogous to reducing the thickness (L) of the sensing film, thereby enhancing the sensor response. This process was recently proven by an experimental study in which the sensor response was significantly improved by using a porous structure with meso- and macroporosity, as shown in Figure 4 [77].
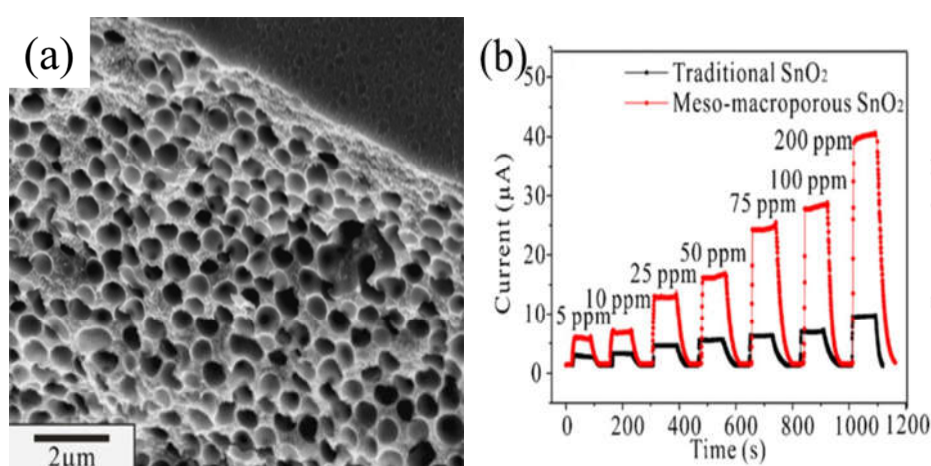
Figure 4. (**a**) SEM image of meso-macroporous SnO₂; (**b**) Real-time responses of the sensors based on meso-macroporous SnO₂ and traditional SnO₂, respectively. Reprinted from [77] with permission.

4.2. Effect of the Defects

Defects have crucial impacts on the physical characteristics and electronic structures of semiconductor metal oxides, thereby playing an important role in the sensing reaction. Previous reports have shown that defects are beneficial to the improvement of sensitivity. Notably, manipulating the defect structures of semiconductor metal oxides can effectively enhance the

gas-sensing performance. Li et al. established a relation between the defect structure and the sensor response. ZnO nanosheets were prepared by the precipitation method at different calcination temperatures (200, 400 and 600 °C), which were exploited to detect acetone. Li et al. found that the ZnO nanosheets, which had been calcined at 200 °C, showed high acetone sensitivity [78]. The superior performance might be attributed to the morphology, grain size, specific surface area and surface defect content. Notably, the shape and grain size of the ZnO nanosheets did not change below 400 °C. As a consequence, these influencing factors were ruled out simultaneously. Nevertheless, the specific surface area of ZnO nanosheets at different calcination temperatures was different, and the values could impact the performance. Therefore, the effect of the specific surface area was excluded by normalized the response.

Subsequently, Li et al. studied the correlation between the sensor response and the surface defect content. The sensor response was based on the resistance change caused by the redox reaction between the target gases with the adsorbed oxygen species. The amount of adsorbed oxygen species played an important role in the enhancement of the sensor response. The surface defects could increase the amount of adsorbed oxygen species. ZnO nanosheets calcined at 200 °C exhibited abundant surface defects that could cause more oxygen molecules to be adsorbed on the metal oxide surfaces. This process also meant that more free electrons were captured from the conduction band, leading to a larger L_D, as illustrated in the top right corner of Figure 5a. When the ZnO nanosheets were exposed to acetone gas, more acetone molecules reacted with the adsorbed oxygen species. More electrons were released to the conduction band, thus leading to a smaller L_D and inducing an improved performance, as presented in the bottom right corner of Figure 5a. It could be concluded that the sensor response was related to the surface defect content. As shown in Figure 5b, the normalized defect content decreased with increasing calcination temperature. This phenomenon could be explained by the fact that heat treatment reduced the number of defects. It is reasonable that the reduced number of defects could lead to diminished adsorbed oxygen species, leading to a decrease in the sensor response. Hence, the adsorbed oxygen species reached a maximum with greater surface defect content at the calcination temperature of 200 °C, and the sensor response reached a maximum as well.
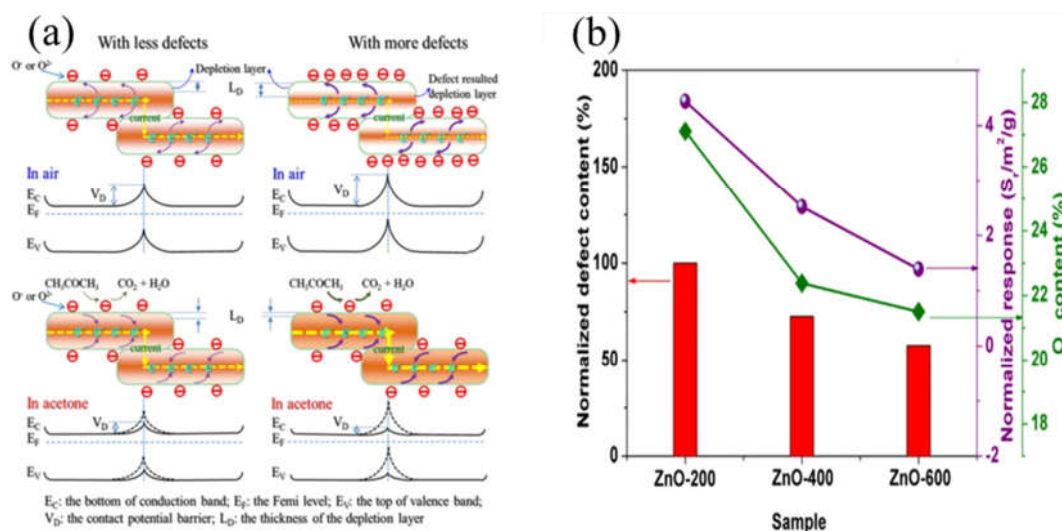
Figure 5. (**a**) Schematic illustration of the contact potential barrier under the electron transfer between two neighboring ZnO nanosheets viewed from the side with less and more defects; (**b**) The normalized defect content, the oxygen species content and the normalized response to 200 ppm acetone vapor at 300 °C. Reprinted from [78] with permission.

4.3. Effect of the Catalyst

The catalytic influence on semiconductor metal oxides results in the acceleration of the interaction between adsorbed oxygen species and target gases. Generally, noble metal is introduced

into semiconductor metal oxides as a sensitizer or activator [79]. This is because the noble metal can affect the inter-granular contact region and thereby change the resistance of the gas sensor in two ways, namely, chemical sensitization and electronic sensitization. Liu et al. demonstrated that the sensor based on Pt-loaded α-Fe$_2$O$_3$ porous nanospheres exhibited a higher response to acetone than the sensor based on pure α-Fe$_2$O$_3$ samples [80]. For chemical sensitization, Pt was used as a catalyst to promote the formation of more active sites and the dissociation of oxygen molecules. The oxygen ions can be easily enriched and then spill over onto the surface of α-Fe$_2$O$_3$, extracting a greater degree of electrons. For electronic sensitization, Pt played the role of the electron acceptor on the surface of α-Fe$_2$O$_3$. The work function of Pt was higher than that of α-Fe$_2$O$_3$, and the electrons were transferred from α-Fe$_2$O$_3$ to Pt until equilibrium was reached, as shown in Figure 6. The process contributed to developing a wider electron-depleted region and greater band bending at the interface of Pt/α-Fe$_2$O$_3$. The incorporation of Pt into α-Fe$_2$O$_3$ increased the variation in resistance, resulting in an increase in the sensitivity. This finding verifies that noble metal can enhance the gas-sensing performance.
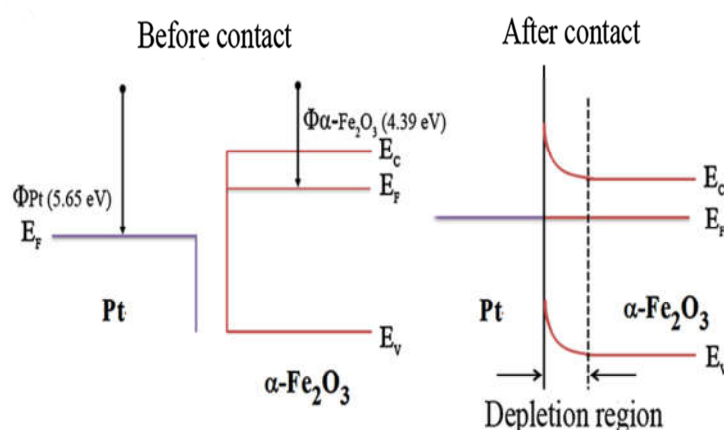
Figure 6. Schematic energy band diagrams of Pt and α-Fe$_2$O$_3$ before/after contact. Reprinted from [80] with permission.

4.4. Effect of the Heterojunction

Heterostructures have attracted great interest due to the different combinations of p-type and n-type semiconductor metal oxides. The interface between two dissimilar semiconductor metal oxides is generally called a heterojunction. Commonly, there is a difference in the Fermi level between two dissimilar semiconductor metal oxides. The electrons flow from the high Fermi level to the low Fermi level until reaching equilibrium, as shown in Figure 7 [25]. This phenomenon can cause the formation of a depletion (or accumulation) region at the interface of heterostructures. The heterojunction can improve the sensitivity of sensors in two different types, including the p–n or n–p junction and the n–n or p–p junction.

Figure 7. *Cont.*

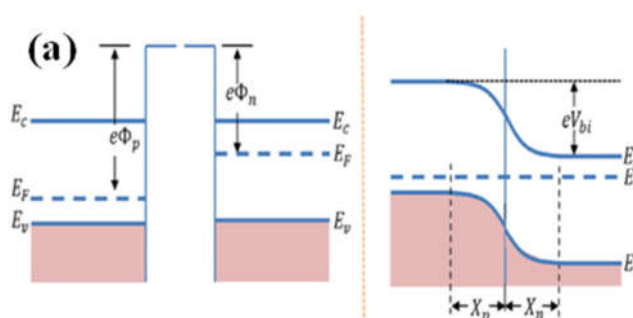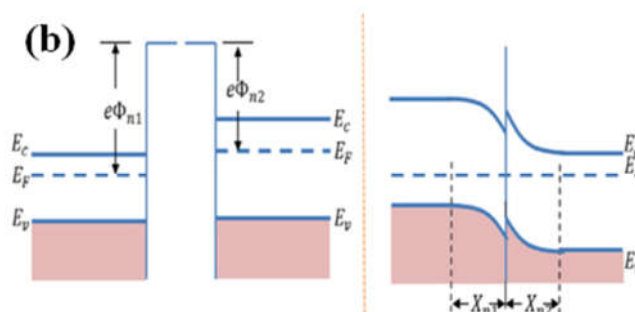**Figure 7.** Schematic diagram showing the possible band structures at (**a**) p–n junction; (**b**) n–n junction. Reprinted from [25] with permission.

4.4.1. p–n or n–p Junction

Semiconductor metal oxides can be divided into two types, namely, p-type and n-type semiconductor metal oxides. There are two combinations of p-type and n-type semiconductor metal oxides in heterojunctions. One is the p–n junction in which an n-type semiconductor metal oxide aids p-type backbones. The other combination is an n–p junction in which a p-type semiconductor metal oxide aids n-type backbones. The major carriers of p-type semiconductors and n-type semiconductors are different. When two different types of semiconductors interact with each other, the electrons in the n-type semiconductors and holes in the p-type semiconductors diffuse in opposite directions [25]. This phenomenon induces a built-in voltage that impedes the flow of charge carriers, thereby increasing the resistance. Xiong et al. prepared ZnO/Co_3O_4 heterostructures with a highly enhanced ethanol sensing performance, which could be interpreted with the p-n heterojunction theory [81]. Due to the adsorption of oxygen, the hole density on the surface of Co_3O_4 increased, whereas the electron density on the surface of ZnO decreased. Hence, it became difficult for the holes to be transferred from Co_3O_4 to ZnO. Upon exposure to ethanol, electrons were released back to the conduction band, resulting in an increased electron density on the surface of ZnO and a decreased hole density on the surface of Co_3O_4. Thus, the number of holes transferred from Co_3O_4 to ZnO was increased, inducing a larger variation in resistance and triggering an enhanced ethanol sensing performance. In addition, the synergistic effect should also be taken into consideration due to the combination of the advantages of two different types of semiconductors. As a result, heterojunctions can improve the gas-sensing performance.

4.4.2. n–n or p–p Junction

Heterojunction can also be formed by the same type of semiconductor metal oxide, namely, n-n or p–p junction. For the p–n junction, there are fewer free electrons at the interface due to electron-hole recombinations, leading to an increase in resistance. However, for the n–n junction, electrons are transferred from a high Fermi level to a low Fermi level, leading to the formation of an accumulation layer. The accumulation layer can be depleted by oxygen molecules, which further increases the potential energy barrier and sensitivity. For instance, Zhang et al. investigated the sensing performance of α-Fe_2O_3/SnO_2 and SnO_2 sensors to ethanol [82]. Notably, the α-Fe_2O_3/SnO_2 sensors exhibited a higher response compared to SnO_2 sensors due to the formation of heterojunctions. Heterostructures endowed them with an additional electron depletion layer at the interface of the heterojunctions, and changed the electron-transport properties.

4.5. Effect of the Humidity

The environmental humidity plays an important role in affecting sensitivity. In fact, the humidity poses an enormous challenge for the development of semiconductor metal oxide gas sensors. This phenomenon can be explained by the large difference in performance between a dry and wet atmosphere. As shown in Figure 8a, the baseline resistance decreases with increasing

humidity. It seems that the level of humidity determines the adsorption rate and thereby changes the sensitivity. The water molecules adsorbed on the semiconductor metal oxide surfaces are involved in the dissociative adsorption reaction and form hydroxyl (OH⁻) and hydrogen (H⁺) ions, as given in Equation (6):

$$H_2O \leftrightarrow OH^- + H^+ \tag{6}$$

Acharyya et al. explained the conduction mechanism based on ZnO nanotubes under the influence of a humid environment, which was related to the chemisorption and physisorption of water molecules on the semiconductor metal oxide surfaces [83]. At a low humidity level, water molecules were chemisorbed at the active sites of semiconductor metal oxide surfaces, leading to the formation of hydroxyl groups absorbed on Zn cations and mobile protons. Moreover, protons reacted with adjacent surface O^{2-}, resulting in secondary hydroxyl ions. The process decreased the baseline resistance in a low humidity environment compared to the case with dry air conditions. At a high humidity level, all active sites were occupied by chemisorbed water molecules, whereby the water molecules were physically adsorbed on the chemisorbed layer, as shown in Figure 8b. With increasing humidity, more multilayer physical adsorptions would be formed on the surface of the ZnO nanotube. Meanwhile, the water molecules in these layers could be ionized to form a large amount of hydronium (H_3O^+) ions under the electrostatic field. A charge transfer was induced by proton hopping between neighbouring water molecules. The process of proton conduction resulted in a lower baseline resistance compared to a low humidity level. Furthermore, water molecules competed with gas molecules at higher humidity level, which decreased the amount of charged oxygen species and hindered the adsorption probability of gas molecules. That is the reason why the sensitivity of gas sensors is reduced under humid conditions. Therefore, controlling the environmental humidity is important for improvement of the gas-sensing performance.
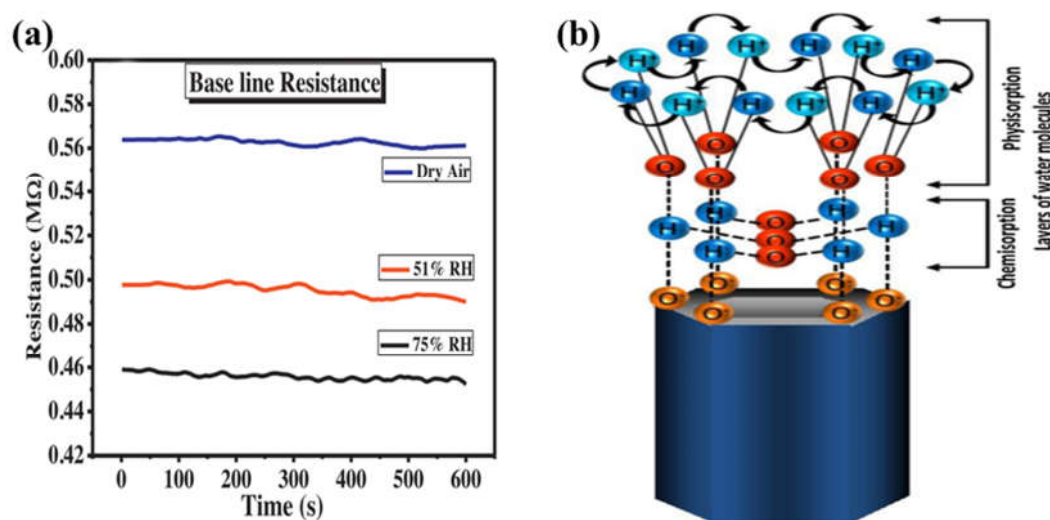
Figure 8. (**a**) Effect of relative humidity on the base line resistance; (**b**) Schematic representation of water molecule adsorption on ZnO nanotube surface. Reprinted from [83] with permission.

5. Semiconductor Metal Oxide Gas Sensors for the Detection of Volatile Organic Compounds

Volatile organic compounds (VOCs) originating from forest fires, vegetation emissions, agricultural respiration, painting, oil refining, vehicle exhaust emissions, and waste material disposal do increasingly serious harm to human life and health. In recent years, many efforts have been devoted to the development of high performance gas sensors for monitoring the air quality. Tables 2–6 list the gas-sensing performances of semiconductor metal oxides, which were influenced by the microstructure, defects, catalyst, heterojunction and humidity, towards ethanol, acetone, formaldehyde, toluene and acetylene. The details are discussed in the following five sections.

5.1. Ethanol Sensors

Ethanol has been widely used in the food industry, automotive fuel industry and manufacture of medicine, specifically for alcohol content monitoring and breath analysis. Drunk driving is extremely dangerous, so the detection of ethanol has an important significance of societal security [84]. Many researchers have investigated the detection of ethanol based on semiconductor metal oxide gas sensors. Table 2 lists the gas-sensing performances of semiconductor metal oxides for ethanol gas. Among the semiconductor metal oxides, SnO_2-based nanomaterials have been considered promising candidates for detecting ethanol gas. Moreover, ternary oxides have also attracted extensive research interest for ethanol sensing.

Table 2. Summary of the gas-sensing performances of semiconductor metal oxides for ethanol gas.

Order	Dimensions	Materials	Synthesis Method	Conc. (ppm)	LOD (ppm)	Temp. (°C)	τ_{res} (s)	τ_{rec} (s)	Resp.	Ref.
1	0D	$CuBi_2O_4$ powders	polymerized complex method	1000	5	400	57	294	10.4 [b]	[85]
2		SnO_2 nanoparticles	microwave treatment	250	NA	100	16	25	30 [c]	[86]
3	1D	Co_3O_4 microrods	interfacial-reaction	100	NA	220	0.8	10.8	9.8 [b]	[87]
4		CuO/In_2O_3 nanorods	thermal evaporation and sputtering	50	NA	300	53	149	3.82 [a]	[88]
5		In_2O_3 microrods	hydrothermal	100	1	300	15	20	18.33 [a]	[89]
6		$LaFeO_3$ nanotubes	electrospinning	100	NA	160	2	4	9.4 [b]	[90]
7		Pd/Fe_2O_3 nanotubes	electrospinning	50	0.1	240	8	30	65.4 [a]	[91]
8		ZnO nanotubes	electrodeposition and electrochemical etching	700	1	RT	4.56 min	1.53 min	64.17% [c]	[83]
9		$LaMnO_3/SnO_2$ nanofibers	electrospinning	100	NA	260	6	34	20 [a]	[92]
10		WO_3/SnO_2 nanofibers	coaxial electrospinning	10	NA	280	18.5	282	5.09 [a]	[93]
11		ZnO nanowires	solvothermal	500	NA	340	6	26	10.68 [a]	[94]
12		SnO_2/Fe_2O_3 nanowires	VLS, hydrothermal and spin coating	5	NA	300	100	300	3.07 [a]	[95]
13		SnO_2/ZnO nanowires	carbon-assisted thermal evaporation	400	NA	400	NA	NA	128 [c]	[96]
14		SnO_2/ZnO nanowires	thermal evaporation and spray-coating	100	NA	400	NA	NA	14.1 [a]	[97]
15	2D	CuO films	RF sputtering	12.5	NA	180	31	52	2.2 [b]	[98]
16		$Pd/Ce/SnO_2$ films	co-precipitation	100	NA	250	6	20	88 [c]	[99]
17		NiO nanosheets	hydrothermal	50	1	240	4	7	11.15 [b]	[100]
18		ZnO nanosheets	hydrothermal	50	1	330	15	12	83.6 [a]	[101]

Table 2. *Cont.*

		Material	Method	Conc.	LOD	Temp.	τ_{res}	τ_{cov}	Resp.	Ref.
19		SnO₂ nanoflowers	hydrothermal	200	4.52	240	10	16	62.2 [a]	[102]
20		SnO₂ nanoflowers	hydrothermal	100	NA	300	10	16	47.29 [a]	[103]
21		Au/SnO₂ hierarchical structures	hydrothermal	100	NA	340	5	10	18 [a]	[104]
22		NiO hierarchical structures	hydrothermal	400	NA	300	4	8	32 [b]	[105]
23		SnO₂ macropores structures	sol-gel method	500	NA	240	NA	NA	70.94 [a]	[106]
24		MoO₃ microboxes	hydrothermal	100	1	260	15	5	78 [a]	[107]
25		SnO₂ nanocubes	hydrothermal	100	1	200	23	21	1670.5 [a]	[108]
26		ZnSnO₃ nanocubes	co-precipitation	100	NA	260	4	276	34.1 [a]	[109]
27		PdO/Zn₂SnO₄ octahedrons	hydrothermal and wet impregnation treatment	100	0.5	250	1	206	82.3 [a]	[110]
28		WO₃ urchin-like structures	hydrothermal	100	NA	350	28	12	68.56 [a]	[111]
29	3D	Co₃O₄ microspheres	interfacial-reaction	100	1	220	0.1	0.7	38.2 [b]	[112]
30		CuO microspheres	precipitation	400	NA	250	17	11.9	5.6 [b]	[113]
31		CuO microspheres	hydrothermal	100	NA	200	2	8	390% [c]	[114]
32		Fe₂O₃/Co₃O₄ microspheres	solution route	100	NA	170	3.3	5.4	16.1 [b]	[115]
33		SnO₂ microspheres	ion exchange method	200	NA	260	NA	NA	103.1 [a]	[116]
34		SnO₂/Fe₂O₃ microspheres	hydrothermal	100	0.1	260	3	4	41.7 [a]	[117]
35		ZnFe₂O₄ microspheres	solvothermal	10	0.5	180	5.1	6.5	6.85 [a]	[118]
36		Pt/SnO₂ nanospheres	spray drying and Kirkendall diffusion	5	0.25	325	1	1577	1399.9 [a]	[119]
37		SnO₂ nanospheres	precipitation	200	NA	260	10	8	274.5 [a]	[120]
38		SnO₂ nanospheres	hydrothermal	100	0.5	350	5	NA	10.5 [a]	[121]
39		SnO₂/ZnO nanospheres	self-sacrificial template	50	NA	270	0.4	235	7.5 [a]	[122]
40		ZnSnO₃ nanospheres	hydrothermal	100	NA	200	4	30	32 [a]	[123]
41		Zn₂SnO₄ nanospheres	hydrothermal	50	5	180	NA	NA	23.4 [a]	[124]

Note: Conc. = concentration; LOD = limit of detection; Temp. = temperature; τ_{res} = response time; τ_{cov} = recovery time; Resp. = Response; Ref. = References; RT = room temperature; [a] $S = R_a/R_g$; [b] $S = R_g/R_a$; [c] $S = (\Delta R/R_a)*100\%$; [d] $S = I_g/I_a$; NA = not available.

Li et al. prepared semi-blooming nanoflowers, blooming SnO₂ nanoflowers and mesoporous semi-blooming SnO₂ nanoflowers using hydrothermal conditions [102]. Among the three nanoflowers, mesoporous semi-blooming SnO₂ nanoflowers were more advantageous to achieve a high response to 200 ppm ethanol due to the largest specific surface area and mesoporous structure.

Their limit of detection reached 4.52 ppm. Therefore, the mesoporous semi-blooming SnO$_2$ nanoflower-based sensor was applied to monitor the presence of beer, as shown in Figure 9. Figure 9a showed that two light-emitting diodes were off when beer was not poured. Then, a green diode would turn on when beer was poured. At the same time, a red diode also turned on, indicating the twinkling warning of the presence of beer, as shown in Figures 9b–d. The experimental results showed that fabricated semi-blooming nanoflower-based sensors can be considered attractive candidates for the determination of drunk driving behaviour.
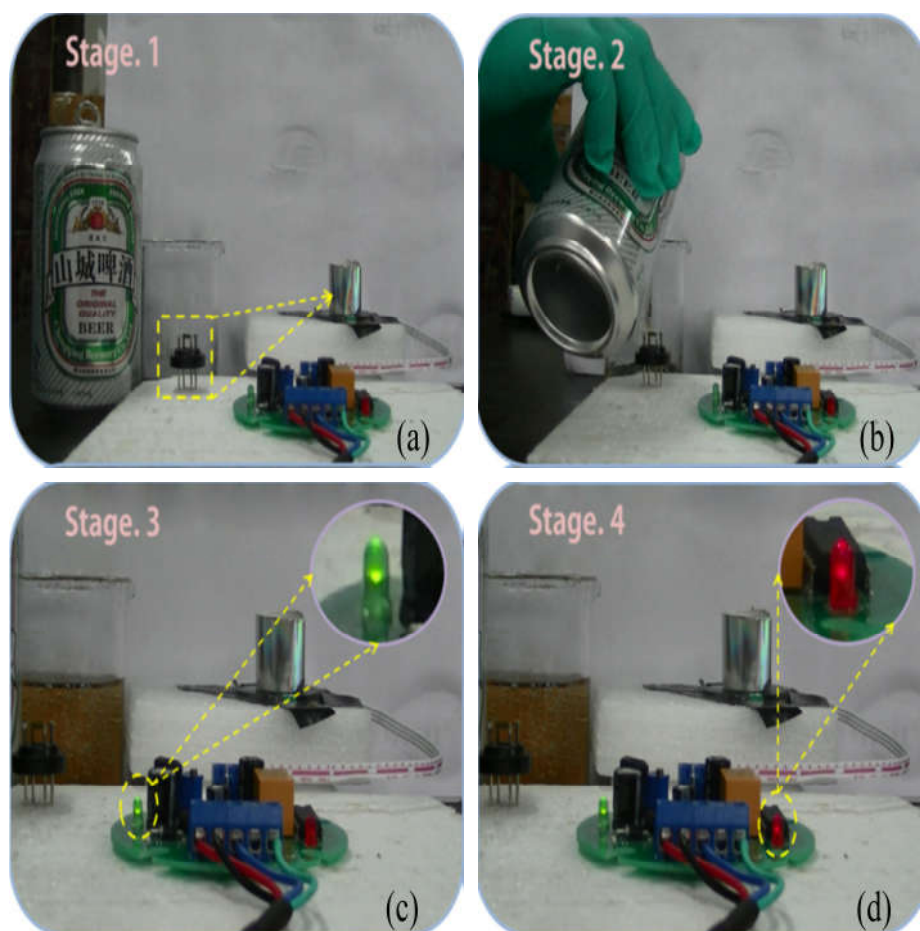

Figure 9. Demonstration of the beer monitoring using the mesoporous semi-blooming SnO$_2$ nanoflowers-based sensor: (**a**) the beer was not poured; (**b**) the beer was poured; (**c**) the green diode turned on; (**d**) the red diode turned on. Reprinted from [102] with permission.

Kim et al. reported Pt-doped SnO$_2$ hollow nanospheres as an ethanol sensor [119]. The Pt-doped SnO$_2$ hollow nanospheres were formed by Kirkendall diffusion. The response of the 0.3 wt.% Pt-doped SnO$_2$ hollow nanosphere-based sensor was 1399.9 to 5 ppm ethanol, which showed a superior selectivity to ethanol due to the excellent catalytic ability of Pt.

SnO$_2$ nanowires coated with Fe$_2$O$_3$ nanoparticles were prepared by Choi et al. using the vapor-liquid-solid (VLS) process, a subsequent hydrothermal method and spin coating [95]. The reported results indicated that the operating temperature was an important factor for enhancing the gas-sensing performance. This finding was because the ionosorption of oxygen and ethanol gas was insufficient at low temperatures. However, the increment of carriers decreased the depletion layer of nanowires, leading to a decreased resistance at high temperatures. The Fe$_2$O$_3$ nanoparticle-coated SnO$_2$ nanowires exhibited a high sensitivity to 200 ppm ethanol at 300 °C with negligible cross-responses to acetone, methanol, toluene and benzene compared to SnO$_2$ nanowires. The improvement of the SnO$_2$/Fe$_2$O$_3$ nanocomposite gas-sensing performance was caused by extending the width of the surface depletion layer at the interface of the heterojunctions.

Recently, ternary oxide-based ethanol sensors have been investigated by many researchers [85,109,118,123–126]. Zhou et al. prepared $ZnSnO_3$ hollow cubes using the co-precipitation method, followed by alkali etching and annealing under inert conditions [109]. The sensor based on $ZnSnO_3$ hollow cubes exhibited a superior response to 100 ppm ethanol at 260 °C, which was 1.77-fold higher than that of the $ZnSnO_3$ solid cube-based sensor. The improved response value was ascribed to the hollow interior structure and porous surface, providing large surface area and excellent permeation. Furthermore, the $ZnSnO_3$ hollow cube-based sensor exhibited a short response time of 4 s. However, the sensor had a relatively long recovery time of 276 s, attributed to the slow dissociation of oxygen and the formation of oxygen species (O^-). Additionally, the $ZnSnO_3$ hollow cube-based sensor showed remarkable selectivity to ethanol compared to other gases, such as C_6H_6, C_7H_8, NH_3, CO and C_3H_6O.

Another ternary oxide has also been investigated for ethanol sensing. Choi et al. applied the polymerized complex method to prepare single-phase polycrystalline $CuBi_2O_4$ and investigated its gas-sensing property with the variation in the calcination temperature [85]. The $CuBi_2O_4$-based sensor with 500 °C-calcined powder was found to be sensitive to C_2H_5OH and showed the highest sensor response with the highest defect concentration. This was because the calcination temperature could change the intrinsic defect concentration, leading to changes in the hole concentration and electronic band gap energy with polaronic hopping conduction.

5.2. Acetone Sensors

Human breath is utilized as a bio marker for various kinds of diseases [127]. Acetone is the endogenous molecule that exists in human breath. The variation in concentration is an indication of disease. For patients with diabetes, acetone can be detected in their breath [128]. Owing to a lack of insulin within the body of the patient with diabetes, fat is used as energy rather than glucose. The accumulation of ketones during metabolic activity leads to a higher acetone concentration in the expiration gas of patients with diabetes. For a fast and easy diagnosis of diabetes, there have been many researchers who have focused on the detection of the least concentration of acetone in breath. Table 3 lists the acetone sensing performances of different semiconductor metal oxides. From most reported data, ZnO, $ZnFe_2O_4$ and Fe_2O_3 have been demonstrated to be the most promising potential materials for acetone sensing.

Table 3. Summary of the gas-sensing performances of semiconductor metal oxides for acetone gas.

Order	Dimensions	Materials	Synthesis Method	Conc. (ppm)	LOD (ppm)	Temp. (°C)	τ_{res} (s)	τ_{rec} (s)	Resp.	Ref.
1		Au/ZnO nanoparticles	MOF template	10	0.05	280	15	12	43 [a]	[129]
2		Ce/CoFe₂O₄ nanocrystallites	molten-salt	2000	NA	200	38	61	157 [b]	[130]
3	0D	Fe₂O₃ nanoparticles	hard template	100	NA	300	6	NA	26.3 [a]	[131]
4		Pt/In₂O₃ nanoparticles	sol-gel	1.56	0.01	200	25	120	12 [a]	[132]
5		ZnFe₂O₄ nanoparticles	hydrothermal	200	NA	200	NA	NA	39.5 [a]	[133]
6		LaFeO₃ powders	sol-gel method	10	NA	200	21	6	7.83 [b]	[134]
7		Co₃O₄ nanochains	solution route	200	5	180	32	35	10.5 [b]	[135]
8	1D	Fe₂O₃ nanorods	interfacial-reaction	100	NA	280	0.4	2.4	32.5 [a]	[136]
9		ZnFe₂O₄ nanorods	hydrothermal	100	NA	260	1	11	52.8 [a]	[137]
10		Fe₂O₃ nanotubes	electrospinning	100	NA	240	9	3	11 [a]	[138]

Table 3. *Cont.*

				Conc.	LOD	Temp.	τ_{res}	τ_{cov}	Resp.	Ref.
11	2D	Co$_3$O$_4$ nanosheets	fluorine-assisted hydrothermal	1000	NA	111	NA	NA	36.5 [b]	[139]
12		ZnO nanosheets	precipitation	200	0.81	300	18.71	13.75	106.1 [a]	[78]
13		In$_2$O$_3$ films	sparking process	2000	NA	350	3	NA	117 [a]	[140]
14		ZnO films	sol-gel dip coating	50	2	RT	60	28	490 [a]	[141]
15		ZnO films	e-beam and post-annealing	100	10	280	6	18	30 [a]	[9]
16	3D	Fe$_2$O$_3$ microflowers	hydrothermal	100	NA	220	8	19	52 [a]	[142]
17		SnO$_2$ nanoflowers	hydrothermal	50	NA	170	3	28	29.2 [a]	[143]
18		ZnO nanoflowers	hydrothermal	100	NA	300	7	NA	18.6 [a]	[144]
19		ZnFe$_2$O$_4$/ZnO microflowers	solution route	50	1	250	2	25	8.3 [a]	[145]
20		ZnO porous flowers	hydrothermal	50	0.25	280	2	23	97.8 [a]	[146]
21		LaFeO$_3$ microspheres	hydrothermal	100	1	225	5	25	25.5 [b]	[147]
22		Au/In$_2$O$_3$ nanospheres	hydrothermal	10	NA	320	4	9	53.08 [b]	[148]
23		LaFeO$_3$ microspheres	hydrothermal	100	NA	260	9	17	29 [b]	[149]
24		SnO$_2$/Fe$_2$O$_3$ nanospheres	self-sacrificial template	100	NA	260	3	6	47.1 [a]	[150]
25		ZnFe$_2$O$_4$ nanospheres	solvothermal	30	0.8	200	9	272	11.8 [a]	[151]
26		ZnFe$_2$O$_4$ microspheres	solvothermal	50	0.5	200	NA	NA	28.3 [a]	[152]
27		ZnFe$_2$O$_4$ microspheres	hydrothermal	20	0.13	206	NA	NA	13.6 [a]	[153]
28		ZnO/ZnFe$_2$O$_4$ microspheres	self-sacrificial template	20	NA	140	5.2	12.8	5.9 [a]	[154]
29		SnO$_2$ hierarchical structures	hydrothermal	100	0.05	325	NA	NA	175 [a]	[155]
30		ZnO macro-mesoporous structures	layer-by-layer filtration deposition	100	NA	260	13	50	137 [a]	[156]
31		ZnO urchin-like structures	hydrothermal	10	NA	300	42	10	58.1 [a]	[157]
32		ZnO/ZnFe$_2$O$_4$ microcubes	MOF template	5	0.5	250	5.6 min	6.0 min	9.4 [a]	[158]
33		ZnFe$_2$O$_4$ octahedral nanocages	thermal decomposition	200	NA	120	NA	NA	64.4 [a]	[159]
34		ZnO/ZnFe$_2$O$_4$ nanocages	self-sacrificial template	100	1	290	8	32	25.8 [a]	[160]

Note: Conc. = concentration; LOD = limit of detection; Temp. = temperature; τ_{res} = response time; τ_{cov} = recovery time; Resp. = Response; Ref. = References; RT = room temperature; [a] $S = R_a/R_g$; [b] $S = R_g/R_a$; [c] $S = (\Delta R/R_a)*100\%$; [d] $S = I_g/I_a$; NA = not available.

3D interconnected macro-mesoporous ZnO (3D-IMM-ZnO) nanostructures were prepared by the layer-by-layer filtration deposition method, which was exploited to detect acetone [156]. Liu et al. found that the sensor response value of 3D-IMM-ZnO nanostructures with the largest macropores was approximately 137, which was higher compared to ZnO nanoparticles and other

3D-IMM-ZnO nanostructures. The superior performance might be attributed to the macropores in the 3D-IMM-ZnO nanostructure accelerating gas accessibility, resulting in the acetone molecules sufficiently contacting the ZnO nanoparticles. In addition, 3D-IMM-ZnO nanostructures with the largest macropores could provide the largest cavities for gas diffusion, inducing faster electron transmission compared to other 3D-IMM-ZnO nanostructures.

Zhang et al. synthesized $ZnFe_2O_4$ nanoparticles by tuning the mole ratio of ZnO to $FeCl_3$ under hydrothermal conditions [133]. The mixture of ZnO and $ZnFe_2O_4$ was obtained by changing the mole ratio from 6:1 to 1:1. Notably, the content of $ZnFe_2O_4$ increased with decreasing mole ratio. When the mole ratio of ZnO to $FeCl_3$ was 1:2, well-dispersed $ZnFe_2O_4$ nanoparticles with no other impurity phases were obtained for acetone sensing investigation. Compared to the precursor ZnO nanoparticle-based sensor, the $ZnFe_2O_4$ nanoparticle-based sensor reduced the power consumption. In addition, the $ZnFe_2O_4$ nanoparticle-based sensor exhibited improved gas-sensing properties, which were ascribed to the smaller size and higher surface area.

Song et al. reported triple-shell heterojunctional hollow microspheres for acetone detection based on a combination of ZnO and $ZnFe_2O_4$ [154]. The acetone sensing properties of $ZnO/ZnFe_2O_4$ heterostructures were investigated systematically. Apparently, the novel heterostructure exhibited the best response value towards acetone at an ultralow working temperature (140 °C) compared to other gases, as shown in Figure 10a. The enhanced response of $ZnO/ZnFe_2O_4$ triple-shell hollow microspheres was explained by the synergistic effect of ZnO and $ZnFe_2O_4$. The heterostructures ensured the effective electrical contact between ZnO and $ZnFe_2O_4$, which reduced the potential barrier and facilitated electron transport at low temperatures. This phenomenon prompted more adsorbed oxygen species to participate in the reaction, thereby improving the sensitivity. Figure 10b showed the resistance transient of the $ZnO/ZnFe_2O_4$ triple-shell hollow microsphere-based sensor towards 20 ppm acetone. The response and recovery times were approximately 5.2 and 12.8 s, respectively. The fast response/recovery speed was attributed to the porous and triple-shell hollow structures that were conducive to gas diffusion.
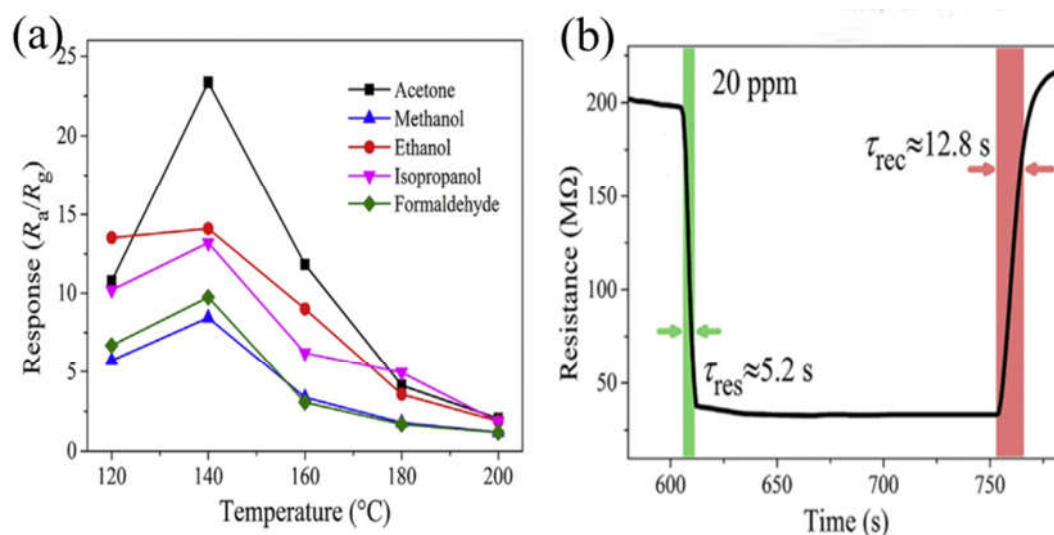

Figure 10. (**a**) Response of the sensor based on $ZnO/ZnFe_2O_4$ heterostructures to different gases (200 ppm) at different working temperatures; (**b**) Resistance transient of the sensor towards 20 ppm acetone. Reprinted from [154] with permission.

Additionally, the excellent sensing performance may be ascribed to three key factors proposed by Yamazoe et al., including the receptor function, the transducer function and the utility factor of the sensing body [161]. First, the multishell hollow structures of $ZnO/ZnFe_2O_4$ were receptive to more oxygen molecules, providing a significant reactive boost. Second, the spheres were composed of interconnected nanoparticles. The particle size was small enough and was twice the thickness of the space charge layer, thereby achieving complete depletion (transducer function). Third, the

porous hollow structures and the voids between the three shells were favourable for the permeability and diffusion of acetone gases (utility factor), which was responsible for an improved response.

More recently, Fe_2O_3 has attracted much attention as a sensing material. Wang et al. prepared microsheet-assembled Fe_2O_3 microflowers by employing a hydrothermal method based on different concentrations of Fe^{3+} precursor solutions (0.025, 0.020, 0.015 and 0.010 mol/L Fe^{3+}) [142]. The thickness of the microsheet became thinner with decreasing concentrations of Fe^{3+}, increasing the porosity of the Fe_2O_3 microflowers. However, some of the microflowers could break up into particles and decreased in uniformity when the concentration of Fe^{3+} was 0.010 mol/L, which had agreat impact on the sensing performance. Thus, the 0.015 mol/L Fe^{3+} sample exhibited a high response with a value of 52 as well as a fast response and recovery times of 8 and 19 s, respectively. The excellent performance was attributed to the high surface area and numerous porous structures.

5.3. Formaldehyde Sensors

HCHO is considered one of the most common hazardous gases and is identified as a carcinogen. In daily life, many activities release varying amounts of HCHO into the atmosphere [162]. The release of formaldehyde not only harms health but also restricts sustainable development. To solve environmental problems, an increasing number of researchers have tried to develop high performance gas sensors for the detection of formaldehyde. In Table 4, we summarize the gas-sensing performances of various semiconductor metal oxides for detecting HCHO gas. Among them, In_2O_3, NiO and SnO_2 are the most promising semiconductor metal oxides for the monitoring of formaldehyde.

Table 4. Summary of the gas-sensing performances of semiconductor metal oxides for formaldehyde gas.

Order	Dimensions	Materials	Synthesis Method	Conc. (ppm)	LOD (ppm)	Temp. (°C)	τ_{res} (s)	τ_{rec} (s)	Resp.	Ref.
1		In_2O_3 particles	hydrothermal	50	NA	130	37	48	86 [a]	[163]
2	0D	In_2O_3 nanoparticles	hydrothermal	10	NA	280	4	8	20 [a]	[164]
3		In_2O_3 nanoparticles	hydrothermal	100	NA	230	100	70	80 [a]	[165]
4		NiO nanoparticles	electrodeposition	1	NA	230	53.7	13.3	3.43 [b]	[166]
5	1D	NiO nanochains	electrospinning	50	1	210	1	10	NA	[167]
6		SnO_2 microtubes	solvothermal	100	0.01	92	NA	NA	26.2 [a]	[168]
7	2D	ZnO nanosheets	hydrothermal	50	NA	350	9	11	37.8 [a]	[169]
8		CeO_2 polyhedron	hydrothermal	150	1	220	21	16	172 [a]	[170]
9		In_2O_3 polyhedrons	solution route	20	NA	240	1	2	8.2 [a]	[171]
10		SnO_2 cedar-like structures	hydrothermal	100	1	200	1	13	13.3 [a]	[172]
11		Au/In_2O_3 nanocubes	hydrothermal	100	NA	240	3	8	37 [b]	[173]
12	3D	$ZnSnO_3$ multishelled cubes	coprecipitation and alkaline etching route	100	NA	220	1	59	37.2 [a]	[174]
13		NiO nanotetrahedra	solvothermal	50	NA	250	NA	NA	11.6 [b]	[175]
14		In_2O_3 hierarchical structures	solution route	100	1	260	1	8	8.6 [a]	[176]
15		In_2O_3 microflowers	hydrothermal/solvothermal	50	0.5	190	25	65	90 [a]	[177]
16		NiO microflowers	solvothermal	100	NA	200	30	56	3.5 [b]	[178]

Table 4. *Cont.*

17	CuO microspheres	hydrothermal	100	NA	300	26	28	3.2 [b]	[179]
18	In_2O_3 microspheres	thermal decomposition	50	10	175	25	104	30 [a]	[180]
19	In_2O_3 microspheres	self-sacrificial template	100	NA	300	21	7	40.9 [a]	[181]
20	SnO_2 microspheres	hydrothermal	200	1	300	NA	NA	9 [a]	[182]

Note: Conc. = concentration; LOD = limit of detection; Temp. = temperature; τ_{res} = response time; τ_{cov} = recovery time; Resp. = Response; Ref. = References; RT = room temperature; [a.] $S = R_a/R_g$; [b] $S = R_g/R_a$; [c] $S = (\Delta R/R_a)*100\%$; [d] $S = I_g/I_a$; NA = not available.

Gu et al. investigated In_2O_3 nanoparticles for the improvement of formaldehyde sensing by manipulating the defect structure, such as the oxygen vacancies (V_O) [165]. In_2O_3 nanoparticles with different contents of V_O were obtained by tuning the treatment time (10–30 min). In_2O_3-H10 exhibited the highest response (80) to formaldehyde with a fast response/recovery time (100 s/70 s). The excellent formaldehyde sensing performance was attributed to the greatest bulk quantity of V_O. Moreover, In_2O_3-H10 had a narrower band gap and lower energy barrier due to the formation of new energy levels in the band gap induced by the increment in bulk V_O content, accelerating the electron mobility.

Zhang et al. reported an enhanced sensing performance of Au-loaded In_2O_3 porous nanocubes for formaldehyde detection [173]. The Au-loaded In_2O_3 porous nanocubes were fabricated by a hydrothermal method followed by thermal treatment. The sensitivity of Au-loaded In_2O_3 nanocubes was 2-fold higher than that of pure In_2O_3 nanocubes. Moreover, the incorporation of elemental Au reduced the optimum operating temperature. The improved sensing performance was explained by the effect of the catalyst including chemical sensitization and electronic sensitization. For the chemical sensitization, Au was added to In_2O_3 nanocubes as sensitizers. Owing to the spillover effect, it could promote more active sites on the surface of In_2O_3 nanocubes and induce more adsorption of oxygen molecules. For the electronic sensitization, Au acted as an electron acceptor on the surface of In_2O_3, leading to a broader electron-depleted region and greater band bending. Therefore, the incorporation of elemental Au was beneficial to an improved formaldehyde sensing performance.

Except for n-type semiconductor metal oxides, p-type semiconductor metal oxides for formaldehyde sensing have also received much attention owing to their suitable catalytic effect. For instance, Fu et al. prepared tetrahedron-like NiO nanostructures by a solvothermal reaction followed by calcination at different temperatures (400–600 °C) [175]. NiO nanotetrahedra annealed at 500 °C showed an excellent sensitivity to formaldehyde compared with other annealing temperatures. The sensitivity of p-type semiconductors was related to the concentration of cation vacancies. For the NiO nanotetrahedra, nickel vacancies were formed during the annealing of the NiO precursor. NiO nanotetrahedra annealed at 500 °C had a relatively higher nickel vacancy concentration, leading to improved sensitivity. Meanwhile, the sample had a relatively larger specific surface area, which was favourable for the adsorption of more oxygen molecules.

Most semiconductor metal oxides have superior responses to ppm-level formaldehyde at low working temperatures. However, the ppb-level concentration detection of HCHO at low working temperatures is more important for people due to threat it poses to the health. Recently, Zhang et al. applied a solvothermal method to synthesize SnO_2 microtubes, which exhibited a low limit of detection (10 ppb) and a high response to HCHO at a low temperature of 92 °C with negligible cross-responses to CO, C_6H_6, C_6H_7N, NH_3, C_3H_6O and C_2H_5OH, as shown in Figure 11 [168]. In addition, the sensor response of the microtubes was remarkably higher compared to irregular spheres, which was ascribed to the adsorption of more HCHO molecules caused by the hollow structure and rapid electron transfer provided by a direct path in the tubes.
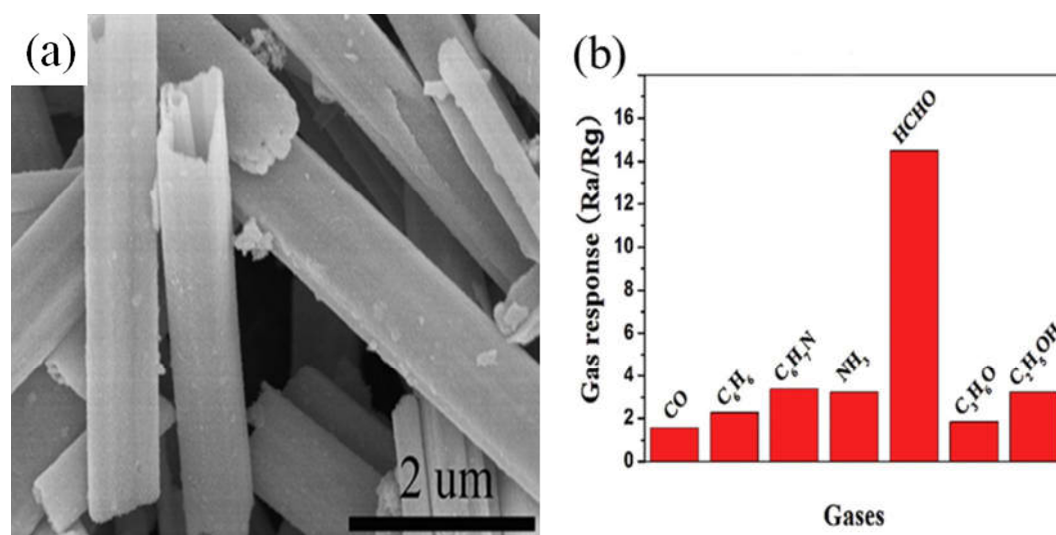
Figure 11. (**a**) SEM image of SnO_2 microtubes; (**b**) Responses of the sensor to 50 ppm CO, C_6H_6, C_6H_7N, NH_3, HCHO, C_3H_6O and C_2H_5OH operated at 92 °C. Reprinted from [168] with permission.

5.4. Toluene Sensors

C_7H_8 is considered a kind of biomarker in human breath arising from the process of metabolism. Biomarkers can intuitively show abnormalities within the body. Lung cancer can be reflected by the gaseous toluene biomarker in exhaled breath [183]. Thus, toluene sensors can be used for non-invasive disease diagnostics through the detection of gaseous biomarkers. Recently, many gas sensors have been developed in the field of detecting toluene. As shown in Table 5, SnO_2-based nanostructures have often been investigated for the detection of toluene. Great efforts surrounding the addition of noble metals and metal oxides to SnO_2 nanomaterials have been devoted to improving the toluene sensing performance.

Table 5. Summary of the gas-sensing performances of semiconductor metal oxides for toluene gas.

Order	Dimensions	Materials	Synthesis Method	Conc. (ppm)	LOD (ppm)	Temp. (°C)	τ_{res} (s)	τ_{rec} (s)	Resp.	Ref.
1	0D	Au/ZnO nanoparticles	coprecipitation	100	NA	377	NA	6 min	92 [a]	[184]
2		Pd/SnO₂ nanofibers	electrospinning and carbonization	100	0.5	250	3	35	24.6 [a]	[185]
3		Pd/WO₃ nanofibers	electrospinning	1	0.02	350	10.9	16.1	5.5 [b]	[186]
4		Pt/SnO₂/ZnO nanowires	vapor-liquid-solid, atomic layer deposition and γ-ray radiolysis	0.1	NA	300	NA	NA	279 [a]	[187]
5	1D	TiO₂ nanotubes	hydrothermal	50	NA	500	110–130	800–1150	3 [a]	[188]
6		ZnO nanowires	electrospinning and hydrothermal	100	1	240	9	4	12.7 [a]	[189]
7		Fe₂O₃/NiO nanotubes	hydrothermal	5	0.5	275	10	24	8.8 [b]	[190]
8		SnO₂/Fe₂O₃ nanotubes	electrospinning	50	0.05	260	5	11	25.3 [a]	[191]
9		Fe₂O₃/SnO₂ nanowires	ultrasonic spray pyrolysis and hydrothermal	100	NA	90	20	15	49.7% [c]	[192]
10		Co₃O₄ nanorods	solvothermal	200	NA	200	90	55	35 [b]	[193]

Table 5. *Cont.*

11		$MoO_3/Fe_2(MoO_4)_3$ nanobelts	hydrothermal	50	NA	250	NA	NA	5.3 [a]	[194]
12		Pd/SnO_2 microspheres	hydrothermal	20	0.1	230	0.48	5.5	52.9 [a]	[195]
13		In_2O_3 microspheres	hydrothermal	50	0.5	350	12	25	85% [c]	[196]
14		Au/TiO_2 pecan-kernel-like structures	hydrothermal and precipitation	100	NA	375	4	5	7.3 [a]	[197]
15	3D	Pd/SnO_2 cubic nanocages	self-sacrificial template and precipitation	20	0.1	230	0.4	16.5	41.4 [a]	[198]
16		SnO_2 nanocages	self-sacrificial template	20	NA	250	2.3	5.8	33.4 [a]	[199]
17		PdO/ZnO nanoflowers	hydrothermal	100	NA	240	1	9	10.9 [a]	[200]
18		SnO_2/SnO_2 cuboctahedra	anneal-etching	20	NA	250	1.8	4.1	28.6 [a]	[201]
19		$ZnFe_2O_4$ nanospheres	nonaqueous route	100	1	300	18.14	29.2	9.98 [a]	[202]

Note: Conc. = concentration; LOD = limit of detection; Temp. = temperature; τ_{res} = response time; τ_{cov} = recovery time; Resp. = Response; Ref. = References; RT = room temperature; [a] $S = R_a/R_g$; [b] $S = R_g/R_a$; [c] $S = (\Delta R/R_a)*100\%$; [d] $S = I_g/I_a$; NA = not available.

Bing et al. reported the synthesis of solid SnO_2 cubes, single-shell SnO_2 cages and yolk-shell SnO_2 cuboctahedras for the detection of toluene [201]. The sensor response towards 20 ppm toluene at 250 °C was increased from 12.1 for solid SnO_2 cubes and 22.4 for single-shell SnO_2 cages to 28.6 for yolk-shell SnO_2 cuboctahedra, as shown in Figure 12. In addition, yolk-shell SnO_2 cuboctahedra exhibited the fastest response and recovery times of 1.8 and 4.1 s, respectively.
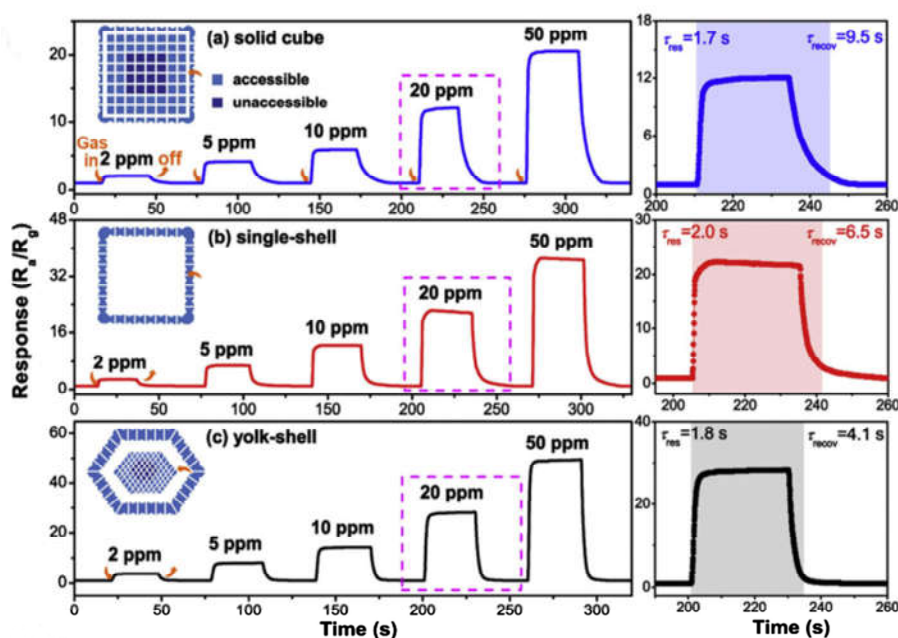

Figure 12. Dynamic toluene sensing transients of SnO_2 products with (**a**) solid cubes; (**b**) single-shell structures; (**c**) yolk-shell structures to toluene with different concentrations. The right insets show the corresponding response time (res) and recovery time (recov) examined to 20 ppm toluene, respectively. Reprinted from [201] with permission.

The exceptional gas-sensing performance of yolk-shell SnO_2 cuboctahedra was attributed to a special hierarchical architecture with a core@void@shell configuration. The distinctive structures provided penetrable shells and cores for fast mass transfer as well as multiple walls for an increased surface area.

Xie et al. synthesized pristine SnO_2, pristine Pd/SnO_2 and carbonized Pd/SnO_2 nanofibers by electrospinning for toluene sensing [185]. They reported that the pristine Pd/SnO_2 sensors exhibited a higher response and lower operating temperature compared to the pristine SnO_2 sensors due to the chemical and electronic sensitizations caused by the catalyst Pd. After carbonization treatment, the carbonized Pd/SnO_2 nanofibers showed a higher response compared to the pristine Pd/SnO_2 nanofibers owing to the porous structure and the enhancement of the chemisorbed oxygen (O_c). On the one hand, Pd/SnO_2 nanofibers with carbonization possessed porous structures that were beneficial for gas diffusion into the inner-surface/outer-surface. On the other hand, the oxidation and reduction reaction of carbon species might lower the oxygen supply to Sn during the formation of SnO_2 particles. Moreover, the combustion of carbon species might also consume a portion of the oxygen atoms coming from the SnO_2 particles. Hence, more chemisorbed oxygens could participate in the reaction due to the formation of more oxygen defects compared with the traditional method, thereby enhancing the sensor response to toluene.

Kim et al. reported the exceptional sensing performance of Pt-functionalized SnO_2/ZnO core/shell nanowires for detecting ppb-levels of toluene [187]. To verify the superior toluene sensing characteristics of Pt-functionalized SnO_2/ZnO core/shell nanowires, ZnO nanowires, SnO_2 nanowires and SnO_2/ZnO core/shell nanowires were also prepared for the detection of toluene. After comparison, it could be found that the SnO_2/ZnO core/shell nanowires showed enhanced properties compared to the two single component semiconductor metal oxide nanowires due to the formation of a heterointerface between SnO_2 and ZnO. The sensor response of the heterostructure varied with the thickness of the shell due to the radial modulation of the electron-depleted shell layer. Therefore, the toluene response was further improved by controlling the thickness of the shell. Furthermore, Pt-functionalized SnO_2/ZnO core/shell nanowires with a shell thickness of 80 nm exhibited an excellent sensor response value of 279 for 100 ppb toluene and outstanding selectivity in the presence of interfering gases including CO, CO_2, and C_6H_6. The catalytic effect of Pt nanoparticles might not only promote more interactions between the gaseous molecules but also dissociate the toluene gas more effectively relative to the other interfering gases. Moreover, the attachment of Pt nanoparticles to the ZnO shell layer could cause the flow of electrons from the ZnO shell layer to the Pt nanoparticles according to the Fermi level difference, leading to a further improvement of the sensing performance.

5.5. Acetylene Sensors

Acetylene is an explosive and flammable volatile organic compound. Therefore, it is of great significance to detect acetylene gas in industrial production, chemical processing, cutting metals and welding. For environmental monitoring and safety protection, the development of high efficiency acetylene sensors has drawn attention [203,204]. The acetylene sensing performances of semiconductor metal oxides are rarely reported but highly meaningful. Table 6 summarizes the acetylene sensing properties of semiconductor metal oxides. ZnO is the most promising candidate for acetylene sensors.

Qiao et al. prepared mesoporous ZnO nanosheets by the hydrothermal method [205]. They reported that ZnO nanosheets-based sensors exhibited superior acetylene sensing performance at the optimum operating temperature of 400 °C with a response (R_a/R_g) of 164.3 for 200 ppm acetylene. In particular, the sensor could detect 1 ppm acetylene with a high response value (R_a/R_g = 10). In addition, it was noteworthy that a level of 1 ppm acetylene could be detected at 285 °C below the autoignition temperature of acetylene (305 °C) with a response value of 4, which was high enough for practical applications ($R_a/R_g \geq 3$).

Table 6. Summary of the gas-sensing performances of semiconductor metal oxides for acetylene gas.

Order	Dimensions	Materials	Synthesis Method	Conc. (ppm)	LOD (ppm)	Temp. (°C)	τ_{res} (s)	τ_{rec} (s)	Resp.	Ref.
1		Pt/ZnO nanoparticles	flame spray pyrolysis	10000	NA	300	6	60	836 [a]	[206]
2	0D	Ag/ZnO/RGO hybrid nanostructures	chemical route	100	1	150	25	80	21.2 [a]	[207]
3		Sm$_2$O$_3$/SnO$_2$ nanorods	hydrothermal	100	NA	260	8	9	50.5 [a]	[208]
4	1D	WO$_3$ nanowires	hydrothermal	200	NA	300	6	7	58 [a]	[209]
5		Au/ZnO/In$_2$O$_3$ belt-tooth	chemical vapor deposition	100	NA	90	8.5	NA	5 [a]	[210]
6	2D	ZnO nanosheets	hydrothermal	100	1	400	11	5	101.1 [a]	[205]
7		Au/ZnO nanorings	hydrothermal and deposition	100	0.5	255	4	3	28 [a]	[211]
8		ZnO nanoflowers	hydrothermal	200μL/L	NA	375	8	11	48.2 [a]	[212]
9		Au/ZnO microspheres	hydrothermal and precipitation	100	1	183.5	8	2	311.3 [a]	[213]
10	3D	NiO/SnO$_2$ hierarchical structures	hydrothermal	100	1	206	2	5	13.8 [a]	[214]
11		Ag/ZnO/RGO hierarchical structures	photochemical	100	3	200	57	90	12.3 [a]	[215]

Note: Conc. = concentration; LOD = limit of detection; Temp. = temperature; τ_{res} = response time; τ_{cov} = recovery time; Resp. = Response; Ref. = References; RT = room temperature; [a] $S = R_a/R_g$; [b] $S = R_g/R_a$; [c] $S = (\Delta R/R_a)*100\%$; [d] $S = I_g/I_a$; NA = not available.

The structural sensitization involved morphology and defect effects, enhancing the gas-sensing performance of the ZnO nanosheet-based sensors. First, mesoporous nanosheets possessed large specific surface area and mesoporous feature, contributing to the increased adsorption capacity of gas molecules and improved gas diffusion. Additionally, the thickness of the ZnO nanosheets was nearly identical to two times the Debye length, leading to almost fully depleted electrons and a remarkably enhanced sensor response. Second, the abundant intrinsic defects present in the mesoporous ZnO nanosheets could absorb more oxygen molecules and subsequently ionize them. It meant that a broader depletion layer was generated, resulting in an enhanced acetylene sensing property.

Uddin et al. investigated Ag-loaded hierarchical ZnO-reduced graphene oxide (Ag/ZnO Hrc-RGO) hybrids and Ag-loaded ZnO-reduced graphene oxide (Ag/ZnO-Gr) hybrids as sensing materials for acetylene sensing at low temperatures, as shown in Figures 13a,b [207,215]. They found that the Ag/ZnO-Gr hybrid nanostructures exhibited a higher response value and faster response time compared to the Ag/ZnO Hrc-RGO hybrid nanostructures. The higher response could be explained by the ZnO nanoparticles in the Ag/ZnO-Gr hybrids having larger surface area, more uniform shape, smaller grain size and better crystallinity compared with the ZnO hierarchical nanostructures in the Ag/ZnO Hrc-RGO hybrids. In addition, the enhanced sensing property of the Ag/ZnO-Gr hybrids towards acetylene might be caused by the improved contacts among the Ag nanoparticles, ZnO nanoparticles and thin nanosheets of the reduced graphene oxides.

In addition, they also reported the humidity effect on the gas-sensing properties of Ag/ZnO-Gr hybrid nanostructures and Ag/ZnO Hrc-RGO hybrid nanostructures, as shown in Figures 13c,d. It should be noted that water molecules could affect the properties of gas sensors. The response decreased with increasing RH concentration. This phenomenon was because water molecules decreased the adsorption of chemisorbed oxygen species, resulting in chemisorbed hydroxide (OH$^-$)

on the surface of sensing materials. The process reduced the surface area and decreased the C_2H_2 adsorption, leading to deterioration of the response.
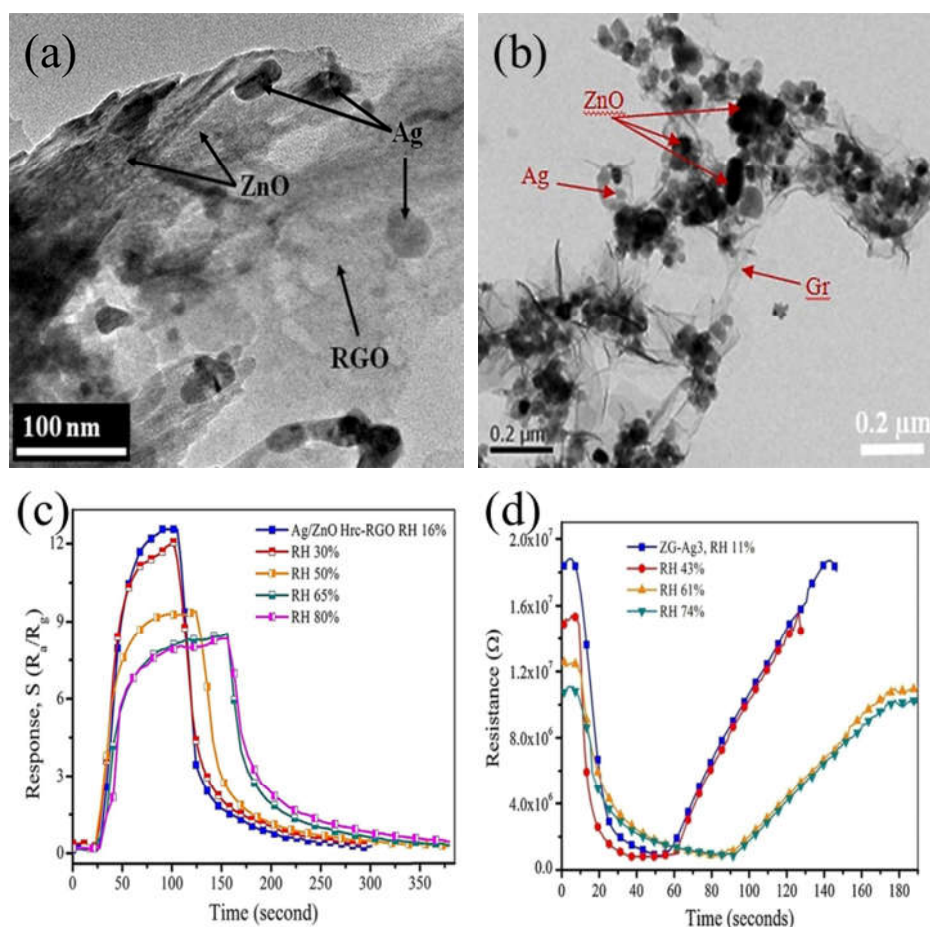

Figure 13. TEM images of (**a**) Ag-loaded hierarchical ZnO-reduced graphene oxide hybrid; (**b**) Ag-loaded ZnO-reduced graphene oxide hybrid; Transient response at different humidity concentrations of (**c**) Ag-loaded hierarchical ZnO-reduced graphene oxide hybrid; (**d**) Ag-loaded ZnO-reduced graphene oxide hybrid. Reprinted from [207, 215] with permission.

6. Conclusions and Outlook

In this review, the general properties of VOCs and the gas-sensing mechanism of chemoresistive semiconductor metal oxide gas sensors are described to better understand the necessity of detecting VOCs and the operating principle of gas sensors. Then, five factors that affect the sensitivity, including the microstructure, defects, catalyst, heterojunction and humidity, were introduced. Subsequently, the developments of semiconductor metal oxide gas sensors for detecting five common VOCs, such as ethanol, acetone, formaldehyde, toluene and acetylene, were reviewed from the perspective of the five factors above. From most reported data, it can be concluded that ZnO, SnO_2, Fe_2O_3, In_2O_3 and NiO are the most promising semiconductor metal oxides for detecting VOCs.

Although many researchers have committed to fabricating high performance gas sensors, there is still room for further improvement of the gas sensitivity. Except for the sensing materials, gas sensor devices need to be improved for practical applications, particularly with respect to reliability and durability. Accuracy and robustness tests should also be carried out for the sake of security. With the global environment worsening, it is imperative that continuous research should be conducted to improve the sensor performance in detecting hazardous gases. Undoubtedly, the improvement of gas sensors will continue to play an important role in the future.

References

1.　Wang, H.L.; Nie, L.; Li, J.; Wang, Y.F.; Wang, G.; Wang, J.H.; Hao, Z.P. Characterization and assessment of volatile organic compounds (VOCs) emissions from typical industries. *Chin. Sci. Bull.* **2013**, *58*, 724–730.

2.　Ralf, K. Volatile Organic Compounds in the Atmosphere, Blackwell: Oxford, UK, 2007; pp. 1-500.

3.　Ren, F.; Gao, L.; Yuan, Y.; Zhang, Y.; Alqrni, A.; Al-Dossary, O.M.; Xu, J. Enhanced BTEX gas-sensing performance of CuO/SnO$_2$ composite. *Sens. Actuators B Chem.* **2016**, *223*, 914–920.

4.　Yan, H.; Song, P.; Zhang, S.; Zhang, J.; Yang, Z.; Wang, Q. Au nanoparticles modified MoO3 nanosheets with their enhanced properties for gas sensing. *Sens. Actuators B Chem.* **2016**, *236*, 201–207.

5.　Liu, X.; Iocozzia, J.; Wang, Y.; Cui, X.; Chen, Y.; Zhao, S.; Li, Z.; Lin, Z. Noble metal-metal oxide nanohybrids with tailored nanostructures for efficient solar energy conversion, photocatalysis and environmental remediation. *Energ Environ Sci.* **2017**, *10*, 402–434.

6.　Arafat, M.M.; Haseeb, A.S.M.A.; Akbar, S.A.; Quadir, M.Z. In-situ fabricated gas sensors based on one dimensional core-shell TiO$_2$-Al$_2$O$_3$ nanostructures. *Sens. Actuators B Chem.* **2017**, *238*, 972–984.

7.　Majhi, S.M.; Rai, P.; Yu, Y.T. Facile Approach to Synthesize Au@ZnO Core-Shell Nanoparticles and Their Application for Highly Sensitive and Selective Gas Sensors. *ACS Appl. Mater. Interfaces* **2015**, *7*, 9462–9468.

8.　Moran-Lazaro, J.P.; Lopez-Urias, F.; Munoz-Sandoval, E.; Blanco-Alonso, O.; Sanchez-Tizapa, M.; Carreon-Alvarez, A.; Guillen-Bonilla, H.; Olvera-Amador, M.L.; Guillen-Bonilla, A.; Rodriguez-Betancourtt, V.M. Synthesis, Characterization, and Sensor Applications of Spinel ZnCo$_2$O$_4$ Nanoparticles. *Sensors* **2016**, *16*, 1–14.

9.　Teimoori, F.; Khojier, K.; Dehnavi, N.Z. Investigation of sensitivity and selectivity of ZnO thin film to volatile organic compounds. *J. Theor. Appl. Phys.* **2017**, *11*, 157–163.

10.　Feng, C.; Wang, C.; Zhang, H.; Li, X.; Wang, C.; Cheng, P.; Ma, J.; Sun, P.; Gao, Y.; Zhang, H.; Sun, Y.; Zheng, J.; Lu, G. Enhanced sensitive and selective xylene sensors using W-doped NiO nanotubes. *Sens. Actuators B Chem.* **2015**, *221*, 1475–1482.

11.　Wang, L.; Li, J.; Wang, Y.; Yu, K.; Tang, X.; Zhang, Y.; Wang, S.; Wei, C. Construction of 1D SnO$_2$-coated ZnO nanowire heterojunction for their improved n-butylamine sensing performances. *Sci. Rep.* **2016**, *6*, 1–12.

12.　Wang, L.; Zhang, R.; Zhou, T.; Lou, Z.; Deng, J.; Zhang, T. Concave Cu$_2$O octahedral nanoparticles as an advanced sensing material for benzene (C$_6$H$_6$) and nitrogen dioxide (NO$_2$) detection. *Sens. Actuators B Chem.* **2016**, *223*, 311–317.

13.　Zeng, Q.Z.; Ma, S.Y.; Jin, W.X.; Yang, H.M.; Chen, H.; Ge, Q.; Ma, L. Hydrothermal synthesis of monodisperse α-Fe$_2$O$_3$ hollow microspheroids and their high gas-sensing properties. *J. Alloys Compd.* **2017**, *705*, 427–437.

14.　Bonyani, M.; Lee, J.K.; Sun, G.-J.; Lee, S.; Ko, T.; Lee, C. Benzene sensing properties and sensing mechanism of Pd-decorated Bi$_2$O$_3$-core/ZnO-shell nanorods. *Thin Solid Films* **2017**, *636*, 257–266.

15.　Vesely, P.; Lusk, L.; Basarova, G.; Seabrooks, J.; Ryder, D. Analysis of aldehydes in beer using solid-phase microextraction with on-fiber derivatization and Gas Chromatography/Mass Spectrometry. *J. Agric. Food Chem.* **2003**, *51*, 6941–6944.

16.　Teixeira, L.S.; Leao, E.S.; Dantas, A.F.; Pinheiro, H.L.; Costa, A.C.; de Andrade, J.B. Determination of formaldehyde in Brazilian alcohol fuels by flow-injection solid phase spectrophotometry. *Talanta* **2004**, *64*, 711–715.

17.　Kumar, P.; Deep, A.; Kim, K.H.; Brown, R.J.C. Coordination polymers: Opportunities and challenges for monitoring volatile organic compounds. *Prog. Polym. Sci.* **2015**, *45*, 102–118.

18.　Wei, Y.; Wang, X.; Yi, G.; Zhou, L.; Cao, J.; Sun, G.; Chen, Z.; Bala, H.; Zhang, Z. Hydrothermal synthesis of Ag modified ZnO nanorods and their enhanced ethanol-sensing properties. *Mat. Sci. Semicond. Proc.* **2018**, *75*, 327–333.

19. Wang, X.; Gao, M., Porous Co_3O_4/SnO_2 quantum dot (QD) heterostructures with abundant oxygen vacancies and Co^{2+} ions for highly efficient gas sensing and oxygen evolution reaction. *Nanoscale* **2018**, *10*, 12045–12053.

20. Liu, X.; Jiang, L.; Jiang, X.; Tian, X.; Sun, X.; Wang, Y.; He, W.; Hou, P.; Deng, X.; Xu, X. Synthesis of Ce-doped In_2O_3 nanostructure for gas sensor applications. *Appl. Surf. Sci.* **2018**, *428*, 478–484.

21. Li, F.; Ruan, S.; Zhang, N.; Yin, Y.; Guo, S.; Chen, Y.; Zhang, H.; Li, C. Synthesis and characterization of Cr-doped WO_3 nanofibers for conductometric sensors with high xylene sensitivity. *Sens. Actuators B Chem.* **2018**, *265*, 355–364.

22. Feng, C.; Kou, X.; Chen, B.; Qian, G.; Sun, Y.; Lu, G. One-pot synthesis of in doped NiO nanofibers and their gas sensing properties. *Sens. Actuators B Chem.* **2017**, *253*, 584–591.

23. Kim, J.H.; Lee, J.H.; Mirzaei, A.; Kim, H.W.; Kim, S.S. SnO_2 (n)-NiO (p) composite nanowebs: Gas sensing properties and sensing mechanisms. *Sens. Actuators B Chem.* **2018**, *258*, 204–214.

24. Han, X.; Sun, Y.; Feng, Z.; Zhang, G.; Chen, Z.; Zhan, J. Au-deposited porous single-crystalline ZnO nanoplates for gas sensing detection of total volatile organic compounds. *RSC Adv.* **2016**, *6*, 37750–37756.

25. Li, T.; Zeng, W.; Wang, Z. Quasi-one-dimensional metal-oxide-based heterostructural gas-sensing materials: A review. *Sens. Actuators B Chem.* **2015**, *221*, 1570–1585.

26. Fine, G.F.; Cavanagh, L.M.; Afonja, A.; Binions, R. Metal oxide semi-conductor gas sensors in environmental monitoring. *Sensors* **2010**, *10*, 5469–5502.

27. Lin, T.; Lv, X.; Li, S.; Wang, Q. The Morphologies of the Semiconductor Oxides and Their Gas-Sensing Properties. *Sensors* **2017**, *17*, 1–30.

28. Sun, Y.F.; Liu, S.B.; Meng, F.L.; Liu, J.Y.; Jin, Z.; Kong, L.T.; Liu, J.H. Metal oxide nanostructures and their gas sensing properties: A review. *Sensors* **2012**, *12*, 2610–2631.

29. Mirzaei, A.; Kim, J.H.; Kim, H.W.; Kim, S.S. Resistive-based gas sensors for detection of benzene, toluene and xylene (BTX) gases: A review. *J. Mater. Chem. C* **2018**, *6*, 4342–4370.

30. Wang, C.; Yin, L.; Zhang, L.; Xiang, D.; Gao, R. Metal oxide gas sensors: Sensitivity and influencing factors. *Sensors* **2010**, *10*, 2088–2106.

31. Wetchakun, K.; Samerjai, T.; Tamaekong, N.; Liewhiran, C.; Siriwong, C.; Kruefu, V.; Wisitsoraat, A.; Tuantranont, A.; Phanichphant, S. Semiconducting metal oxides as sensors for environmentally hazardous gases. *Sens. Actuators B Chem.* **2011**, *160*, 580–591.

32. Kim, H.J.; Lee, J.H. Highly sensitive and selective gas sensors using p-type oxide semiconductors: Overview. *Sens. Actuators B Chem.* **2014**, *192*, 607–627.

33. Mirzaei, A.; Leonardi, S.G.; Neri, G. Detection of hazardous volatile organic compounds (VOCs) by metal oxide nanostructures-based gas sensors. *Ceram. Int.* **2016**, *42*, 15119–15141.

34. Khalil, A.; Kim, J.J.; Tuller, H.L.; Rutledge, G.C.; Hashaikeh, R. Gas sensing behavior of electrospun nickel oxide nanofibers: Effect of morphology and microstructure. *Sens. Actuators B Chem.* **2016**, *227*, 54–64.

35. Gurlo, A. Nanosensors: Towards morphological control of gas sensing activity. SnO_2, In_2O_3, ZnO and WO_3 case studies. *Nanoscale* **2011**, *3*, 154–165.

36. Kabcum, S.; Tammanoon, N.; Wisitsoraat, A.; Tuantranont, A.; Phanichphant, S.; Liewhiran, C. Role of molybdenum substitutional dopants on H_2S-sensing enhancement of flame-spray-made SnO_2 nanoparticulate thick films. *Sens. Actuators B Chem.* **2016**, *235*, 678–690.

37. Downie, N.A.; Maran & Co. *Industrial Gases*; Kluwer Academic: New York, NY, USA, 2002; pp. 1–559.

38. Kuwahara, M.; Nishioka, M.; Yoshida, M.; Fujita, K.I. A Sustainable Method for the Synthesis of Acetic Acid Based on Dehydrogenation of an Ethanol-Water Solution Catalyzed by an Iridium Complex Bearing a Functional Bipyridonate Ligand. *ChemCatChem* **2018**, *10*, 3636–3640.

39. Chua, J.Y.; Lu, Y.; Liu, S.Q. Evaluation of five commercial non-Saccharomyces yeasts in fermentation of soy (tofu) whey into an alcoholic beverage. *Food Microbiol.* **2018**, *76*, 533–542.

40. Van Opstaele, F.; Goiris, K.; De Rouck, G.; Aerts, G.; De Cooman, L. Production of novel varietal hop aromas by supercritical fluid extraction of hop pellets-Part 2: Preparation of single variety floral, citrus, and spicy hop oil essences by density programmed supercritical fluid extraction. *J. Supercrit. Fluid* **2012**, *71*, 147–161.

41. Leonardi, S.G.; Mirzaei, A.; Bonavita, A.; Santangelo, S.; Frontera, P.; Panto, F.; Antonucci, P.L.; Neri, G. A comparison of the ethanol sensing properties of alpha-iron oxide nanostructures prepared via the sol-gel and electrospinning techniques. *Nanotechnology* **2016**, *27*, 075502.

42. Lian, X.; Li, Y.; Tong, X.; Zou, Y.; Liu, X.; An, D.; Wang, Q. Synthesis of Ce-doped SnO_2 nanoparticles and their acetone gas sensing properties. *Appl. Surf. Sci.* **2017**, *407*, 447–455.

43. Cheng, L.; Ma, S.Y.; Wang, T.T.; Luo, J., Synthesis and enhanced acetone sensing properties of 3D porous flower-like SnO_2 nanostructures. *Mater. Lett.* **2015**, *143*, 84–87.

44. Koo, W.T.; Yu, S.; Choi, S.J.; Jang, J.S.; Cheong, J.Y.; Kim, I.D., Nanoscale PdO Catalyst Functionalized Co_3O_4 Hollow Nanocages Using MOF Templates for Selective Detection of Acetone Molecules in Exhaled Breath. *ACS Appl. Mater. Interfaces* **2017**, *9*, 8201–8210.

45. Ge, W.; Chang, Y.; Natarajan, V.; Feng, Z.; Zhan, J.; Ma, X. In_2O_3-SnO_2 hybrid porous nanostructures delivering enhanced formaldehyde sensing performance. *J. Alloys Compd.* **2018**, *746*, 36–44.

46. Gu, C.; Cui, Y.; Wang, L.; Sheng, E.; Shim, J.J.; Huang, J. Synthesis of the porous NiO/SnO_2 microspheres and microcubes and their enhanced formaldehyde gas sensing performance. *Sens. Actuators B Chem.* **2017**, *241*, 298–307.

47. Wei, W.; Guo, S.; Chen, C.; Sun, L.; Chen, Y.; Guo, W.; Ruan, S. High sensitive and fast formaldehyde gas sensor based on Ag-doped $LaFeO_3$ nanofibers. *J. Alloys Compd.* **2017**, *695*, 1122–1127.

48. Shen, Z.; Zhang, X.; Ma, X.; Mi, R.; Chen, Y.; Ruan, S. The significant improvement for BTX (benzene, toluene and xylene) sensing performance based on Au-decorated hierarchical ZnO porous rose-like architectures. *Sens. Actuators B Chem.* **2018**, *262*, 86–94.

49. Kawamura, K.; Vestergaard, M.D.; Ishiyama, M.; Nagatani, N.; Hashiba, T.; Tamiya, E. Development of a novel hand-held toluene gas sensor: Possible use in the prevention and control of sick building syndrome. *Measurement* **2006**, *39*, 490–496.

50. Sui, L.; Zhang, X.; Cheng, X.; Wang, P.; Xu, Y.; Gao, S.; Zhao, H.; Huo, L., Au-Loaded Hierarchical MoO_3 Hollow Spheres with Enhanced Gas-Sensing Performance for the Detection of BTX (Benzene, Toluene, And Xylene) And the Sensing Mechanism. *ACS Appl. Mater. Interfaces* **2017**, *9*, 1661–1670.

51. Chen, W.D.; Burie, J.; Boucher D. Investigation on infrared laser absorption spectroscopy measurement of acetylene trace quantities. *Infrared Phys. Technol.* **2000**, *41*, 339–348.

52. Zhang, L.; Zhao, J.; Zheng, J.; Li, L.; Zhu, Z. Hydrothermal synthesis of hierarchical nanoparticle-decorated ZnO microdisks and the structure-enhanced acetylene sensing properties at high temperatures. *Sens. Actuators B Chem.* **2011**, *158*, 144–150.

53. Li, C.; Su, Y.; Lv, X.; Xia, H.; Wang, Y. Electrochemical acetylene sensor based on Au/MWCNTs. *Sens. Actuators B Chem.* **2010**, *149*, 427–431.

54. Wang, J.; Zeng, W.; Wang, Z. Assembly of 2D nanosheets into 3D flower-like NiO: Synthesis and the influence of petal thickness on gas-sensing properties. *Ceram. Int.* **2016**, *42*, 4567–4573.

55. Yuliarto, B.; Gumilar, G.; Septiani, N.L.W. SnO_2 Nanostructure as Pollutant Gas Sensors: Synthesis, Sensing Performances, and Mechanism. *Adv. Mater. Sci. Eng.* **2015**, *2015*, 1–14.

56. Wang, Z.; Wang, D.; Sun, J., Controlled synthesis of defect-rich ultrathin two-dimensional WO_3 nanosheets for NO_2 gas detection. *Sens. Actuators B Chem.* **2017**, *245*, 828–834.

57. Shankar, P.; Rayappan,J.B.B. Gas sensing mechanism of metal oxides: The role of ambient atmosphere, type of semiconductor and gases-A review. *Sci. Lett. J.* **2015**, *4*, 1–18.

58. Wang, C.; Li, X.; Feng, C.; Sun, Y.; Lu, G. Nanosheets assembled hierarchical flower-like WO_3 nanostructures: Synthesis, characterization, and their gas sensing properties. *Sens. Actuators B Chem.* **2015**, *210*, 75–81.

59. Wang, S.; Yang, J.; Zhang, H.; Wang, Y.; Gao, X.; Wang, L.; Zhu, Z. One-pot synthesis of 3D hierarchical SnO_2 nanostructures and their application for gas sensor. *Sens. Actuators B Chem.* **2015**, *207*, 83–89.

60. Wang, Y.; Zhang, B.; Liu, J.; Yang, Q.; Cui, X.; Gao, Y.; Chuai, X.; Liu, F.; Sun, P.; Liang, X.; Sun, Y.; Lu, G. Au-loaded mesoporous WO_3: Preparation and n -butanol sensing performances. *Sens. Actuators B Chem.* **2016**, *236*, 67–76.

61. Li, Y.; Chen, N.; Deng, D.; Xing, X.; Xiao, X.; Wang, Y. Formaldehyde detection: SnO_2 microspheres for formaldehyde gas sensor with high sensitivity, fast response/recovery and good selectivity. *Sens. Actuators B Chem.* **2017**, *238*, 264–273.

62. Wei, F.; Zhang, H.; Nguyen, M.; Ying, M.; Gao, R.; Jiao, Z. Template-free synthesis of flower-like SnO_2 hierarchical nanostructures with improved gas sensing performance. *Sens. Actuators B Chem.* **2015**, *215*, 15–23.

63. Chen, M.; Zhang, Y.; Zhang, J.; Li, K.; Lv, T.; Shen, K.; Zhu, Z.; Liu, Q. Facile lotus-leaf-templated synthesis and enhanced xylene gas sensing properties of Ag-LaFeO₃ nanoparticles. *J. Mater. Chem. C* **2018**, *6*, 6138–6145.

64. Song, X.; Xu, Q.; Zhang, T.; Song, B.; Li, C.; Cao, B. Room-temperature, high selectivity and low-ppm-level triethylamine sensor assembled with Au decahedrons-decorated porous α-Fe₂O₃ nanorods directly grown on flat substrate. *Sens. Actuators B Chem.* **2018**, *268*, 170–181.

65. Subbiah, D.K.; Kulandaisamy, A.J.; George, R.B.; Shankar, P.; Mani, G.K.; Jayanth Babu, K.; Rayappan, J.B.B. Nano ceria as xylene sensor-Role of cerium precursor. *J. Alloys Compd.* **2018**, *753*, 771–780.

66. Shi, S.; Zhang, F.; Lin, H.; Wang, Q.; Shi, E.; Qu, F. Enhanced triethylamine-sensing properties of P-N heterojunction Co₃O₄/In₂O₃ hollow microtubes derived from metal-organic frameworks. *Sens. Actuators B Chem.* **2018**, *262*, 739–749.

67. Vijayakumar, Y.; Mani, G.K.; Ponnusamy, D.; Shankar, P.; Kulandaisamy, A.J.; Tsuchiya, K.; Rayappan, J.B.B.; Ramana Reddy, M.V. V₂O₅ nanofibers: Potential contestant for high performance xylene sensor. *J. Alloys Compd.* **2018**, *731*, 805–812.

68. Liu, C.; Lu, H.; Zhang, J.; Gao, J.; Zhu, G.; Yang, Z.; Yin, F.; Wang, C. Crystal facet-dependent p-type and n-type sensing responses of TiO₂ nanocrystals. *Sens. Actuators B Chem.* **2018**, *263*, 557–567.

69. Xu, T.T.; Xu, Y.M.; Zhang, X.F.; Deng, Z.P.; Huo, L.H.; Gao, S. Enhanced H₂S Gas-Sensing Performance of Zn₂SnO₄ Lamellar Micro-Spheres. *Front. Chem.* **2018**, *6*, 1–5.

70. Han, B.; Liu, X.; Xing, X.; Chen, N.; Xiao, X.; Liu, S.; Wang, Y. A high response butanol gas sensor based on ZnO hollow spheres. *Sens. Actuators B Chem.* **2016**, *237*, 423–430.

71. Gaidan, I.; Brabazon, D.; Ahad, I.U. Response of a Zn₂TiO₄ Gas Sensor to Propanol at Room Temperature. *Sensors* **2017**, *17*, 1–11.

72. Rothschild, A.; Komem, Y. The effect of grain size on the sensitivity of nanocrystalline metal-oxide gas sensors. *J. Appl. Phys.* **2004**, *95*, 6374–6380.

73. Xu, C.N.; Tamaki, J.; Miura, N.; Yamazoe, N. Grain-size effects on gas sensitivity of porous SnO₂-based elements. *Sens. Actuators B Chem.* **1991**, *3*, 147–155.

74. Liang, S.; Li, J.; Wang, F.; Qin, J.; Lai, X.; Jiang, X. Highly sensitive acetone gas sensor based on ultrafine α-Fe₂O₃ nanoparticles. *Sens. Actuators B Chem.* **2017**, *238*, 923–927.

75. Zhang, R.; Zhou, T.; Wang, L.; Zhang, T. Metal-organic frameworks-derived hierarchical Co₃O₄ structures as efficient sensing materials for acetone detection. *ACS Appl. Mater. Interfaces* **2018**, *10*, 9765–9773.

76. Sakai, G.; Matsunaga N.; Shimanoe K.; Yamazoe N. Theory of gas-diffusion controlled sensitivity for thin film senmiconductor gas sensor. *Sens. Actuators B Chem.* **2001**, *80*, 125–131.

77. Li, H.; Meng, F.; Liu, J.; Sun, Y.; Jin, Z.; Kong, L.; Hu, Y.; Liu, J. Synthesis and gas sensing properties of hierarchical meso-macroporous SnO₂ for detection of indoor air pollutants. *Sens. Actuators B Chem.* **2012**, *166-167*, 519-525.

78. Li, S.M.; Zhang, L.X.; Zhu, M.Y.; Ji, G.J.; Zhao, L.X.; Yin, J.; Bie, L.J. Acetone sensing of ZnO nanosheets synthesized using room-temperature precipitation. *Sens. Actuators B Chem.* **2017**, *249*, 611–623.

79. Rai, P.; Majhi, S.M.; Yu, Y.T.; Lee, J.H. Noble metal@metal oxide semiconductor core@shell nano-architectures as a new platform for gas sensor applications. *RSC Adv.* **2015**, *5*, 76229–76248.

80. Liu, C.; Gao, H.; Wang, L.; Wang, T.; Yang, X.; Sun, P.; Gao, Y.; Liang, X.; Liu, F.; Song, H.; Lu, G. Facile synthesis and the enhanced sensing properties of Pt-loaded α-Fe₂O₃ porous nanospheres. *Sens. Actuators B Chem.* **2017**, *252*, 1153–1162.

81. Xiong, Y.; Xu, W.; Zhu, Z.; Xue, Q.; Lu, W.; Ding, D.; Zhu, L. ZIF-derived porous ZnO-Co₃O₄ hollow polyhedrons heterostructure with highly enhanced ethanol detection performance. *Sens. Actuators B Chem.* **2017**, *253*, 523–532.

82. Zhang, B.; Fu, W.; Meng, X.; Ruan, A.; Su, P.; Yang, H. Enhanced ethanol sensing properties based on spherical-coral-like SnO₂ nanorods decorated with α-Fe₂O₃ nanocrystallites. *Sens. Actuators B Chem.* **2018**, *261*, 505–514.

83. Acharyya, D.; Bhattacharyya, P. Alcohol sensing performance of ZnO hexagonal nanotubes at low temperatures: A qualitative understanding. *Sens. Actuators B Chem.* **2016**, *228*, 373–386.

84. Li, L.; Zhang, C.; Zhang, R.; Gao, X.; He, S.; Liu, M.; Li, X.; Chen, W. 2D ultrathin Co₃O₄ nanosheet array deposited on 3D carbon foam for enhanced ethanol gas sensing application. *Sens. Actuators B Chem.* **2017**, *244*, 664–672.

85. Choi, Y.H.; Kim, D.H.; Hong, S.H. CuBi$_2$O$_4$ prepared by the polymerized complex method for gas-sensing applications. *ACS Appl. Mater. Interfaces* **2018**, *10*, 14901–14913.

86. Rajesh, N.; Kannan, J.C.; Krishnakumar, T.; Leonardi, S.G. Neri, G. Sensing behavior to ethanol of tin oxide nanoparticles prepared by microwave synthesis with different irradiation time. *Sens. Actuators B Chem.* **2014**, *194*, 96–104.

87. Tan, W.; Tan, J.; Li, L.; Dun, M.; Huang, X. Nanosheets-assembled hollowed-out hierarchical Co$_3$O$_4$ microrods for fast response/recovery gas sensor. *Sens. Actuators B Chem.* **2017**, *249*, 66–75.

88. Park, S.; Ko, Hy.; An, S.; Lee, W.I.; Lee, S.; Lee, C. Synthesis and ethanol sensing properties of CuO nanorods coated with In$_2$O$_3$. *Ceram. Int.* **2013**, *39*, 5255–5262.

89. Huang, F.; Yang, W.; He, F.; Liu, S. Controlled synthesis of flower-like In$_2$O$_3$ microrods and their highly improved selectivity toward ethanol. *Sens. Actuators B Chem.* **2016**, *235*, 86–93.

90. Zhang, Y.; Duan, Z.; Zou, H.; Ma, M. Fabrication of electrospun LaFeO$_3$ nanotubes via annealing technique for fast ethanol detection. *Mater. Lett.* **2018**, *215*, 58–61.

91. Cheng, Y.; Guo, H.; Wang, Y.; Zhao, Y.; Li, Y.; Liu, L.; Li, H.; Duan, H. Low cost fabrication of highly sensitive ethanol sensor based on Pd-doped α-Fe$_2$O$_3$ porous nanotubes. *Mater. Res. Bull.* **2018**, *105*, 21–27.

92. Chen, D.; Yi, J. One-pot electrospinning and gas-sensing properties of LaMnO$_3$ perovskite/SnO$_2$ heterojunction nanofibers. *J. Nanopart. Res.* **2018**, *20*, 1–10.

93. Li, F.; Gao, X.; Wang, R.; Zhang, T. Design of WO$_3$-SnO$_2$ core-shell nanofibers and their enhanced gas sensing performance based on different work function. *Appl. Surf. Sci.* **2018**, *442*, 30–37.

94. Yuan, Z.; Yin, L.; Ding, H.; Huang, W.; Shuai, C.; Deng, J. One-step synthesis of single-crystalline ZnO nanowires for the application of gas sensor. *J. Mater. Sci. Mater. Electron.* **2018**, *29*, 11559–11565.

95. Choi, K.S.; Park, S.; Chang, S.P. Enhanced ethanol sensing properties based on SnO$_2$ nanowires coated with Fe$_2$O$_3$ nanoparticles. *Sens. Actuators B Chem.* **2017**, 238, 871–879.

96. Tharsika, T.; Haseeb, A.S.; Akbar, S.A.; Sabri, M.F.; Hoong, W.Y., Enhanced ethanol gas sensing properties of SnO$_2$-core/ZnO-shell nanostructures. *Sensors* **2014**, *14*, 14586–14600.

97. Le, D.T.T.; Trung, D.D.; Chinh, N.D.; Binh, B.T.T.; Hong, H.S.; Duy, N.V.; Hoa, N.D.; Hieu, N.V. Facile synthesis of SnO$_2$-ZnO core-shell nanowires for enhanced ethanol-sensing performance. *Curr. Appl. Phys.* **2013**, *13*, 1637–1642.

98. Zoolfakar, A.S.; Ahmad, M.Z.; Rani, R.A.; Ou, J.Z.; Balendhran, S.; Zhuiykov, S.; Latham, K.; Wlodarski, W. Nanostructured copper oxides as ethanol vapour sensors. *Sens. Actuators B Chem.* **2013**, *185*, 620–627.

99. Bagal, L.K.; Patil, J.Y.; Vaishampayan, M.V.; Mulla, I.S.; Suryavanshi, S.S. Effect of Pd and Ce on the enhancement of ethanol vapor response of SnO$_2$ thick films. *Sens. Actuators B Chem.* **2015**, *207*, 383–390.

100. Lu, Y.; Ma, Y.H.; Ma, S.Y.; Jin, W.X.; Yan, S.H.; Xu, X.L.; Chen, Q. Curly porous NiO nanosheets with enhanced gas-sensing properties. *Mater. Lett.* **2017**, *190*, 252–255.

101. Xu, J.; Xue, Z.; Qin, N.; Cheng, Z.; Xiang, Q. The crystal facet-dependent gas sensing properties of ZnO nanosheets: Experimental and computational study. *Sens. Actuators B Chem.* **2017**, *242*, 148–157.

102. Li, T.; Zeng, W.; Long, H.; Wang, Z. Nanosheet-assembled hierarchical SnO$_2$ nanostructures for efficient gas-sensing applications. *Sens. Actuators B Chem.* **2016**, *231*, 120–128.

103. Yu, X.; Zeng, W. Fabrication and gas-sensing performance of nanorod-assembled SnO$_2$ nanostructures. *J. Mater. Sci. Mater. Electron.* **2016**, 27, 7448–7453.

104. Guo, J.; Zhang, J.; Gong, H.; Ju, D.; Cao, B. Au nanoparticle-functionalized 3D SnO$_2$ microstructures for high performance gas sensor. *Sens. Actuators B Chem.* **2016**, *226*, 266–272.

105. Miao, R.; Zeng, W. Hydrothermal synthesis of flake-flower NiO architectures: Structure, growth and gas-sensing properties. *Mater. Lett.* **2016**, *171*, 200–203.

106. Zhang, B.; Fu, W.; Li, H.; Fu, X.; Wang, Y.; Bala, H.; Wang, X.; Sun, G.; Cao, J.; Zhang, Z. Synthesis and characterization of hierarchical porous SnO$_2$ for enhancing ethanol sensing properties. *Appl. Surf. Sci.* **2016**, *363*, 560–565.

107. Zhang, J.; Song, P.; Li, J.; Yang, Z.; Wang, Q. Template-assisted synthesis of hierarchical MoO$_3$ microboxes and their high gas-sensing performance. *Sens. Actuators B Chem.* **2017**, *249*, 458–466.

108. Wang, S.; Yu, W.; Cheng, C.; Zhang, T.; Ge, M.; Sun, Y.; Dai, N. Fabrication of mesoporous SnO$_2$ nanocubes with superior ethanol gas sensing property. *Mater. Res. Bull.* **2017**, *89*, 267–272.

109. Zhou, T.; Zhang, T.; Zhang, R.; Deng, J.; Lou, Z.; Lu, G.; Wang, L. Highly sensitive sensing platform based on ZnSnO$_3$ hollow cubes for detection of ethanol. *Appl. Surf. Sci.* **2017**, *400*, 262–268.

110. Yang, X.; Gao, H.; Zhao, L.; Wang, T.; Sun, P.; Liu, F.; Lu, G. Enhanced gas sensing properties of monodisperse Zn_2SnO_4 octahedron functionalized by PdO nanoparticals. *Sens. Actuators B Chem.* **2018**, *266*, 302–310.

111. Cao, S.; Chen, H. Nanorods assembled hierarchical urchin-like WO_3 nanostructures: Hydrothermal synthesis, characterization, and their gas sensing properties. *J. Alloys Compd.* **2017**, 702, 644–648.

112. Tan, J.; Dun, M.; Li, L.; Zhao, J.; Tan, W.; Lin, Z.; Huang, X. Synthesis of hollow and hollowed-out Co_3O_4 microspheres assembled by porous ultrathin nanosheets for ethanol gas sensors: Responding and recovering in one second. *Sens. Actuators B Chem.* **2017**, *249*, 44–52.

113. Huang, X.; Ren, Z.B.; Zheng, X.H.; Tang, D.P.; Wu, X.; Lin, C. A facile route to batch synthesis CuO hollow microspheres with excellent gas sensing properties. *J. Mater. Sci. Mater. Electron.* **2018**, *29*, 5969–5974.

114. Zhao, Q.; Ma, G.; Zhai, C.; Yang, X.; Zhang, M. Facile synthesis of nanosheets-assembled hierarchical copper oxide microspheres and their ethanol gas sensing properties. *New J. Chem.* **2017**, *41*, 15042–15048.

115. Yang, B.; Liu, J.; Qin, H.; Liu, Q.; Jing, X.; Zhang, H.; Li, R.; Huang, G.; Wang, J. Co_3O_4 nanoparticle-decorated hierarchical flower-like α-Fe_2O_3 microspheres: Synthesis and ethanol sensing properties. *J. Alloys Compd.* **2017**, *727*, 52–62.

116. Wei, Y.; Wang, X.; Yi, G.; Zhou, L.; Cao, J.; Sun, G.; Hari, B. Synthesis and characterization of monodisperse hollow SnO_2 microspheres and their enhanced sensing properties to ethanol. *J. Porous Mater.* **2017**, *25*, 1099–1104.

117. Wang, H.; Wei, S.; Zhang, F.; Li, Y.; Liu, L.; Guo, X.; Song, L. Sea urchin-like SnO_2/Fe_2O_3 microspheres for an ethanol gas sensor with high sensitivity and fast response/recovery. *J. Mater. Sci. Mater. Electron.* **2017**, *28*, 9969–9973.

118. Liu, T.; Liu, J.; Liu, Q.; Rumin, L.; Zhang, H.; Jing, X.; Wang, J. Shape-controlled fabrication and enhanced gas sensing properties of uniform sphere-like $ZnFe_2O_4$ hierarchical architectures. *Sens. Actuators B Chem.* **2017**, *250*, 111–120.

119. Kim, B.Y.; Cho, J.S.; Yoon, J.W.; Na, C.W.; Lee, C.S.; Ahn, J.H.; Kang, Y.C.; Lee, J.H. Extremely sensitive ethanol sensor using Pt-doped SnO_2 hollow nanospheres prepared by Kirkendall diffusion. *Sens. Actuators B Chem.* **2016**, *234*, 353–360.

120. Qiang, Z.; Ma, S.Y.; Jiao, H.Y.; Wang, T.T.; Jiang, X.H.; Jin, W.X.; Yang, H.M.; Chen, H. Highly sensitive and selective ethanol sensors using porous SnO_2 hollow spheres. *Ceram. Int.* **2016**, *42*, 18983–18990.

121. Wang, B.; Sun, L.; Wang, Y. Template-free synthesis of nanosheets-assembled SnO_2 hollow spheres for enhanced ethanol gas sensing. *Mater. Lett.* **2018**, *218*, 290–294.

122. Zhang, R.; Zhou, T.; Wang, L.; Lou, Z.; Deng, J.; Zhang, T. The synthesis and fast ethanol sensing properties of core-shell $SnO_2@ZnO$ composite nanospheres using carbon spheres as templates. *New J. Chem.* **2016**, *40*, 6796–6802.

123. Wang, Q.; Yao, N.; Liu, C.; An, D.; Li, Y.; Zou, Y.; Tong, X. Synthesis of hollow $ZnSnO_3$ nanospheres with high ethanol sensing properties. *J. Nanomater.* **2016**, *2016*, 1–5.

124. An, D.; Mao, N.; Deng, G.; Zou, Y.; Li, Y.; Wei, T.; Lian, X. Ethanol gas-sensing characteristic of the Zn_2SnO_4 nanospheres. *Ceram. Int.* **2016**, *42*, 3535–3541.

125. Jia, X.; Tian, M.; Dai, R.; Lian, D.; Han, S.; Wu, X.; Song, H. One-pot template-free synthesis and highly ethanol sensing properties of $ZnSnO_3$ hollow microspheres. *Sens. Actuators B Chem.* **2017**, *240*, 376–385.

126. Wang, X.; Ding, B.; Liu, Y.; Zhu, X.; Li, H.; Xia, M.; Fu, H.; Li, M. Synthesis of 3D flower-like $ZnSnO_3$ and improvement of ethanol-sensing properties at room temperature based on nano-TiO_2 decoration and UV radiation. *Sens. Actuators B Chem.* **2018**, *264*, 119–127.

127. Staerz, A.; Weimar, U.; Barsan, N. Understanding the Potential of WO_3 Based Sensors for Breath Analysis. *Sensors* **2016**, *16*, 1–16.

128. Gunawan, P.; Mei, L.; Teo, J.; Ma, J.; Highfield, J.; Li, Q.; Zhong, Z., Ultrahigh sensitivity of Au/1D alpha-Fe_2O_3 to acetone and the sensing mechanism. *Langmuir* **2012**, *28*, 14090–14099.

129. Gu, F.; Chen, H.; Han, D.; Wang, Z. Metal–organic framework derived Au@ZnO yolk-shell nanostructures and their highly sensitive detection of acetone. *RSC Adv.* **2016**, *6*, 29727–29733.

130. Khandekara, M.S.; Tarwal, N.L.; Mulla, I.S.; Suryavanshi S. S. Nanocrystalline Ce doped $CoFe_2O_4$ as an acetone gas sensor. *Ceram. Int.* **2014**, *40*, 447–452.

131. Geng, W.; Ge, S.; He, X.; Zhang, S.; Gu, J.; Lai, X.; Wang, H.; Zhang, Q. Volatile organic compound gas-sensing properties of bimodal porous alpha-Fe_2O_3 with ultrahigh sensitivity and fast response. *ACS Appl. Mater. Interfaces* **2018**, *10*, 13702–13711.

132. Karmaoui, M.; Leonardi, S.G.; Latino, M.; Tobaldi, D.M.; Donato, N.; Pullar, R.C.; Seabra, M.P.; Labrincha, J.A.; Neri, G. Pt-decorated In_2O_3 nanoparticles and their ability as a highly sensitive (<10 ppb) acetone sensor for biomedical applications. *Sens. Actuators B Chem.* **2016**, *230*, 697–705.

133. Zhang, J.; Song, J.M.; Niu, H.L.; Mao, C.J.; Zhang, S.Y.; Shen, Y.H. $ZnFe_2O_4$ nanoparticles: Synthesis, characterization, and enhanced gas sensing property for acetone. *Sens. Actuators B Chem.* **2015**, *221*, 55–62.

134. Zhang, H.; Qin, H.; Gao, C.; Zhou, G.; Chen, Y.; Hu, J. UV light illumination can improve the sensing properties of $LaFeO_3$ to acetone vapor. *Sensors* **2018**, *18*, 1–13.

135. Wang, S.; Cao, J.; Cui, W.; Fan, L.; Li, X.; Li, D. Facile synthesis of bamboo raft-like Co_3O_4 with enhanced acetone gas sensing performances. *J. Alloys Compd.* **2018**, *758*, 45–53.

136. Tan, J.; Huang, X. Ultra-thin nanosheets-assembled hollowed-out hierarchical α-Fe_2O_3 nanorods: Synthesis via an interface reaction route and its superior gas sensing properties. *Sens. Actuators B Chem.* **2016**, *237*, 159–166.

137. Li, L.; Tan, J.; Dun, M.; Huang, X. Porous $ZnFe_2O_4$ nanorods with net-worked nanostructure for highly sensor response and fast response acetone gas sensor. *Sens. Actuators B Chem.* **2017**, *248*, 85–91.

138. Guo, X.; Zhang, J.; Ni, M.; Liu, L.; Lian, H.; Wang, H. Comparison of gas sensing properties based on hollow and porous α-Fe_2O_3 nanotubes. *J. Mater. Sci. Mater. Electron.* **2016**, *27*, 11262–11267.

139. Zhang, Z.; Zhu, L.; Wen, Z.; Ye, Z. Controllable synthesis of Co_3O_4 crossed nanosheet arrays toward an acetone gas sensor. *Sens. Actuators B Chem.* **2017**, *238*, 1052–1059.

140. Inyawilert, K.; Wisitsora-at, A.; Tuantranont, A.; Singjai, P.; Phanichphant, S.; Liewhiran C. Ultra-rapid VOCs sensors based on sparked-In_2O_3 sensing films. *Sens. Actuators B Chem.* **2014**, *192*, 745–754.

141. Muthukrishnan, K.; Vanaraja, M.; Boomadevi, S.; Karn, R.K.; Singh, V.; Singh, P.K.; Pandiyan, K. Studies on acetone sensing characteristics of ZnO thin film prepared by sol-gel dip coating. *J. Alloys Compd.* **2016**, *673*, 138–143.

142. Wang, H.; Yan, L.; Li, S.; Li, Y.; Liu, L.; Du, L.; Duan, H.; Cheng, Y. Acetone sensors based on microsheet-assembled hierarchical Fe_2O_3 with different Fe^{3+} concentrations. *Appl. Phys. A* **2018**, *124*, 1–9.

143. Wang, Q.; Yao, N.; An, D.; Li, Y.; Zou, Y.; Lian, X.; Tong, X. Enhanced gas sensing properties of hierarchical SnO_2 nanoflower assembled from nanorods via a one-pot template-free hydrothermal method. *Ceram. Int.* **2016**, *42*, 15889–15896.

144. Peng, C.; Guo, J.; Yang, W.; Shi, C.; Liu, M.; Zheng, Y.; Xu, J.; Chen, P.; Huang, T.; Yang, Y. Synthesis of three-dimensional flower-like hierarchical ZnO nanostructure and its enhanced acetone gas sensing properties. *J. Alloys Compd.* **2016**, *654*, 371–378.

145. Liu, C.; Wang, B.; Wang, T.; Liu, J.; Sun, P.; Chuai, X.; Lu, G. Enhanced gas sensing characteristics of the flower-like $ZnFe_2O_4$/ZnO microstructures. *Sens. Actuators B Chem.* **2017**, *248*, 902–909.

146. Wang, X.; Li, Y.; Liu, L.; Wang, L.; Wang, H.; Guo, X. Synthesis of flower-like porous ZnO and their ultrahigh acetone sensing properties. *J. Porous Mater.* **2016**, *24*, 463–468.

147. Wang, B.; Yu, Q.; Zhang, S.; Wang, T.; Sun, P.; Chuai, X.; Lu, G. Gas sensing with yolk-shell $LaFeO_3$ microspheres prepared by facile hydrothermal synthesis. *Sens. Actuators B Chem.* **2018**, *258*, 1215–1222.

148. Zhang, S.; Song, P.; Zhang, J.; Yan, H.; Li, J.; Yang, Z.; Wang, Q. Highly sensitive detection of acetone using mesoporous In_2O_3 nanospheres decorated with Au nanoparticles. *Sens. Actuators B Chem.* **2017**, *242*, 983–993.

149. Xiao, H.; Xue, C.; Song, P.; Li, J.; Wang, Q. Preparation of porous $LaFeO_3$ microspheres and their gas-sensing property. *Appl. Surf. Sci.* **2015**, *337*, 65–71.

150. Li, H.; Xie, W.; Liu, B.; Wang, Y.; Xiao, S.; Duan, X.; Li, Q.; Wang, T. Ultra-fast and highly-sensitive gas sensing arising from thin SnO_2 inner wall supported hierarchical bilayer oxide hollow spheres. *Sens. Actuators B Chem.* **2017**, *240*, 349–357.

151. Zhou, X.; Liu, J.; Wang, C.; Sun, P.; Hu, X.; Li, X.; Shimanoe, K.; Yamazoe, N.; Lu, G. Highly sensitive acetone gas sensor based on porous $ZnFe_2O_4$ nanospheres. *Sens. Actuators B Chem.* **2015**, *206*, 577–583.

152. Zhou, X.; Wang, B.; Sun, H.; Wang, C.; Sun, P.; Li, X.; Hu, X.; Lu, G. Template-free synthesis of hierarchical $ZnFe_2O_4$ yolk-shell microspheres for high-sensitivity acetone sensors. *Nanoscale* **2016**, *8*, 5446–5453.

153. Qu, F.; Shang, W.; Thomas, T.; Ruan, S.; Yang, M. Self-template derived $ZnFe_2O_4$ double-shell microspheres for chemresistive gas sensing. *Sens. Actuators B Chem.* **2018**, *265*, 625–631.

154. Song, X.Z.; Qiao, L.; Sun, K.M.; Tan, Z.; Ma, W.; Kang, X.L.; Sun, F.F.; Huang, T.; Wang, X.F. Triple-shelled ZnO/$ZnFe_2O_4$ heterojunctional hollow microspheres derived from Prussian Blue analogue as high-performance acetone sensors. *Sens. Actuators B Chem.* **2018**, *256*, 374–382.

155. Li, Y.X.; Guo, Z.; Su, Y.; Jin, X.B.; Tang, X.H.; Huang, J.R.; Huang, X.J.; Li, M.Q.; Liu, J.H. Hierarchical Morphology-Dependent Gas-Sensing Performances of Three-Dimensional SnO_2 Nanostructures. *ACS Sensors* **2016**, *2*, 102–110.

156. Liu, J.; Huang, H.; Zhao, H.; Yan, X.; Wu, S.; Li, Y.; Wu, M.; Chen, L.; Yang, X.; Su, B.L. Enhanced gas sensitivity and selectivity on aperture-controllable 3D interconnected macro-mesoporous ZnO nanostructures. *ACS Appl Mater Interfaces* **2016**, *8*, 8583–8590.

157. Guo, W. One-pot synthesis of urchin-like ZnO nanostructure and its enhanced acetone gas sensing properties. *J. Mater. Sci. Mater. Electron.* **2016**, *28*, 963–972.

158. Ma, X.; Zhou, X.; Gong, Y.; Han, N.; Liu, H.; Chen, Y. MOF-derived hierarchical $ZnO/ZnFe_2O_4$ hollow cubes for enhanced acetone gas-sensing performance. *RSC Adv.* **2017**, *7*, 34609–34617.

159. Song, X.Z.; Meng, Y.L.; Tan, Z.; Qiao, L.; Huang, T.; Wang, X.F. Concave $ZnFe_2O_4$ hollow octahedral nanocages derived from Fe-doped MOF-5 for high-performance acetone sensing at low-energy consumption. *Inorg. Chem.* **2017**, *56*, 13646–13650.

160. Wang, X.; Zhang, S.; Shao, M.; Huang, J.; Deng, X.; Hou, P.; Xu, X. Fabrication of $ZnO/ZnFe_2O_4$ hollow nanocages through metal organic frameworks route with enhanced gas sensing properties. *Sens. Actuators B Chem.* **2017**, *251*, 27–33.

161. Yamazoe, N.; Sakai, G.; Shimanoe, K. Oxide semiconductor gas sensors. *Catal. Surv. Asia* **2003**, *7*, 63–75.

162. Upadhyay, S.B.; Mishra, R.K.; Sahay, P.P. Cr-doped WO_3 nanosheets: Structural, optical and formaldehyde sensing properties. *Ceram. Int.* **2016**, *42*, 15301–15310.

163. Wang, J.; Gan, X.; Li, Z.; Zhou, K. Microstructure and gas sensing property of porous spherical In_2O_3 particles prepared by hydrothermal method. *Powder Technol.* **2016**, *303*, 138–146.

164. Zhang, S.; Song, P.; Yang, Z.; Wang, Q. Facile hydrothermal synthesis of mesoporous In_2O_3 nanoparticles with superior formaldehyde-sensing properties. *Physica E* **2018**, *97*, 38–44.

165. Gu, F.; Li, C.; Han, D.; Wang, Z. Manipulating the defect structure (V_O) of In_2O_3 nanoparticles for enhancement of formaldehyde detection. *ACS Appl. Mater. Interfaces* **2018**, *10*, 933–942.

166. Zhang, Y.; Xie, L.Z.; Yuan, C.X.; Zhang, C.L.; Liu, S.; Peng, Y.Q.; Li, H.R.; Zhang, M. A ppb-level formaldehyde gas sensor based on rose-like nickel oxide nanoparticles prepared using electrodeposition process. *Nano* **2016**, *11*, 1–9.

167. Cao, J.; Zhang, H.; Yan, X. Facile fabrication and enhanced formaldehyde gas sensing properties of nanoparticles-assembled chain-like NiO architectures. *Mater. Lett.* **2016**, *185*, 40–42.

168. Zhang, W.; Cheng, X.; Zhang, X.; Xu, Y.; Gao, S.; Zhao, H.; Huo, L. High selectivity to ppb-level HCHO sensor based on mesoporous tubular SnO_2 at low temperature. *Sens. Actuators B Chem.* **2017**, *247*, 664–672.

169. Guo, W.; Fu, M.; Zhai, C.; Wang, Z., Hydrothermal synthesis and gas-sensing properties of ultrathin hexagonal ZnO nanosheets. *Ceram. Int.* **2014**, *40*, 2295–2298.

170. Hussaina, S.; Aslam, N.; Yang, X.Y.; Javed, M.S.; Xu, Z.W.; Wang, M.S.; Liu, G.W. Qiao, G.J. Unique polyhedron CeO_2 nanostructures for superior formaldehyde gas sensing performances. *Ceram. Int.* **2018**, *44*, 19624–19630.

171. Wang, S.; Cao, J.; Cui, W.; Li, X.; Li, D. Facile synthesis and excellent formaldehyde gas sensing properties of novel spindle-like In_2O_3 porous polyhedra. *Sens. Actuators B Chem.* **2016**, *237*, 944–952.

172. Yu, H.; Yang, T.; Wang, Z.; Li, Z.; Xiao, B.; Zhao, Q.; Zhang, M. Facile synthesis cedar-like SnO_2 hierarchical micro-nanostructures with improved formaldehyde gas sensing characteristics. *J. Alloys Compd.* **2017**, *724*, 121–129.

173. Zhang, S.; Song, P.; Li, J.; Zhang, J.; Yang, Z.; Wang, Q. Facile approach to prepare hierarchical Au-loaded In_2O_3 porous nanocubes and their enhanced sensing performance towards formaldehyde. *Sens. Actuators B Chem.* **2017**, *241*, 1130–1138.

174. Zhou, T.; Zhang, T.; Zhang, R.; Lou, Z.; Deng, J.; Wang, L. Hollow $ZnSnO_3$ cubes with controllable shells enabling highly efficient chemical sensing detection of formaldehyde vapors. *ACS Appl. Mater. Interfaces* **2017**, *9*, 14525–14533.

175. Fu, Q.; Ai, M.; Duan, Y.; Lu, L.; Tian, X.; Sun, D.; Xu, Y.; Sun, Y. Synthesis of uniform porous NiO nanotetrahedra and their excellent gas-sensing performance toward formaldehyde. *RSC Adv.* **2017**, *7*, 52312–52320.

176. Wang, S.; Cao, J.; Cui, W.; Fan, L.; Li, X.; Li, D. Oxygen vacancies and grain boundaries potential barriers modulation facilitated formaldehyde gas sensing performances for In_2O_3 hierarchical architectures. *Sens. Actuators B Chem.* **2018**, *255*, 159–165.

177. Zhang, W.; Zhang, W.; Chen, B.; Shao, R.; Guan, R.; Zhang, W.; Zhang, Q.; Hou, G.; Yue, L. Controllable biomolecule-assisted synthesis and gas sensing properties of In_2O_3 micro/nanostructures with double phases. *Sens. Actuators B Chem.* **2017**, *239*, 270–278.

178. San, X.; Zhao, G.; Wang, G.; Shen, Y.; Meng, D.; Zhang, Y.; Meng, F. Assembly of 3D flower-like NiO hierarchical architectures by 2D nanosheets: Synthesis and their sensing properties to formaldehyde. *RSC Adv.* **2017**, *7*, 3540–3549.

179. Meng, D.; Liu, D.; Wang, G.; San, X.; Shen, Y.; Jin, Q.; Meng, F. CuO hollow microspheres self-assembled with nanobars: Synthesis and their sensing properties to formaldehyde. *Vacuum* **2017**, *144*, 272–280.

180. Zhou, W.; Wu, Y.P.; Wang, X.; Qiao, X.Q.; Hou, D.F.; Zhao, J.; Li, D.S. In-MOFs-derived microsphere In_2O_3 for highly sensitive detecting formaldehyde vapor. *Inorg. Chem. Commun.* **2017**, *85*, 100–104.

181. Zou, Y.; Wang, H.; Lai, X.; Li, X.; Zhou, X.; Lin, G.; Liu, D.; Chen, J.; Xin, H. Synthesis and enhanced formaldehyde-sensing properties of In_2O_3 hollow spheres with thin shells. *J. Electron. Mater.* **2017**, *47*, 2165–2170.

182. Yang, J.; Wang, S.; Dong, R.; Zhang, L.; Zhu, Z.; Gao, X. One-pot synthesis of SnO_2 hollow microspheres and their formaldehyde sensor application. *Mater. Lett.* **2016**, *184*, 9–12.

183. Xing, R.; Xu, L.; Song, J.; Zhou, C.; Li, Q.; Liu, D.; Hong, W. Preparation and gas sensing properties of In_2O_3/Au nanorods for detection of volatile organic compounds in exhaled breath. *Sci. Rep.* **2015**, *5*, 1–14.

184. Suematsu, K.; Watanabe, K.; Tou, A.; Sun, Y.; Shimanoe, K. Ultraselective toluene-gas sensor: Nanosized gold loaded on zinc oxide nanoparticles. *Anal. Chem.* **2018**, *90*, 1959–1966.

185. Xie, N.; Guo, L.; Chen, F.; Kou, X.; Wang, C.; Ma, J.; Sun, Y.; Liu, F.; Liang, X.; Gao, Y.; Yan, X.; Lu, G. Enhanced sensing properties of SnO_2 nanofibers with a novel structure by carbonization. *Sens. Actuators B Chem.* **2018**, *271*, 44–53.

186. Kim, N.H.; Choi, S.J.; Yang, D.J.; Bae, J.; Park, J. Kim I. D. Highly sensitive and selective hydrogen sulfide and toluene sensors using Pd functionalized WO_3 nanofibers for potential diagnosis of halitosis and lung cancer. *Sens. Actuators B Chem.* **2014**, *193*, 574–581.

187. Kim, J.H.; Kim, S.S. Realization of ppb-scale toluene-sensing abilities with Pt-functionalized SnO_2-ZnO core-shell nanowires. *ACS Appl. Mater. Interfaces* **2015**, *7*, 17199–17208.

188. Seo, M.H.; Yuasa, M.; Kida, T. Huh, J.S.; Yamazoe, N. Shimanoe, K. Microstructure control of TiO_2 nanotubular films for improved VOC sensing. *Sens. Actuators B Chem.* **2011**, *154*, 251–256.

189. Sun, Y.; Wei, Z.; Zhang, W.; Li, P.; Lian, K.; Hu, J. Synthesis of brush-like ZnO nanowires and their enhanced gas-sensing properties. *J. Mater. Sci.* **2015**, *51*, 1428–1436.

190. Wang, C.; Wang, T.; Wang, B.; Zhou, X.; Cheng, X.; Sun, P.; Zheng, J.; Lu, G. Design of alpha-Fe_2O_3 nanorods functionalized tubular NiO nanostructure for discriminating toluene molecules. *Sci. Rep.* **2016**, *6*, 1–9.

191. Shan, H.; Liu, C.; Liu, L.; Zhang, J.; Li, H.; Liu, Z.; Zhang, X.; Bo, X.; Chi, X., Excellent toluene sensing properties of SnO_2-Fe_2O_3 interconnected nanotubes. *ACS Appl. Mater. Interfaces* **2013**, *5*, 6376–80.

192. Wang, T.; Huang, Z.; Yu, Z.; Wang, B.; Wang, H.; Sun, P.; Suo, H.; Gao, Y.; Sun, Y.; Li, T.; Lu, G. Low operating temperature toluene sensor based on novel α-Fe_2O_3/SnO_2 heterostructure nanowire arrays. *RSC Adv.* **2016**, *6*, 52604–52610.

193. Wang, L.; Deng, J.; Lou, Z.; Zhang, T., Nanoparticles-assembled Co_3O_4 nanorods p-type nanomaterials: One-pot synthesis and toluene-sensing properties. *Sens. Actuators B Chem.* **2014**, *201*, 1–6.

194. Li, J.; Wang, L.; Liu, H.; Zhao, J.; Li, X.; Wei, H.; Han, Y. Synthesis and enhanced toluene gas sensing properties of 1-D α-MoO_3/$Fe_2(MoO_4)_3$ heterostructure. *J. Alloys Compd.* **2017**, *694*, 939–945.

195. Zhang, K.; Yang, X.; Wang, Y.; Bing, Y.; Qiao, L.; Liang, Z.; Yu, S.; Zeng, Y.; Zheng, W. Pd-loaded SnO_2 ultrathin nanorod-assembled hollow microspheres with the significant improvement for toluene detection. *Sens. Actuators B Chem.* **2017**, *243*, 465–474.

196. Dong, H.; Liu, Y.; Li, G.; Wang, X.; Xu, D.; Chen, Z.; Zhang, T.; Wang, J.; Zhang, L. Hierarchically rosette-like In_2O_3 microspheres for volatile organic compounds gas sensors. *Sens. Actuators B Chem.* **2013**, *178*, 302–309.

197. Zhang, Y.; Li, D.; Qin, L.; Liu, D.; Liu, Y.; Liu, F.; Song, H.; Wang, Y.; Lu, G. Preparation of Au-loaded TiO_2 pecan-kernel-like and its enhanced toluene sensing performance. *Sens. Actuators B Chem.* **2018**, *255*, 2240–2247.

198. Qiao, L.; Bing, Y.; Wang, Y.; Yu, S.; Liang, Z.; Zeng, Y. Enhanced toluene sensing performances of Pd-loaded SnO_2 cubic nanocages with porous nanoparticle-assembled shells. *Sens. Actuators B Chem.* **2017**, *241*, 1121–1129.

199. Bing, Y.; Zeng, Y.; Liu, C.; Qiao, L.; Zheng, W., Synthesis of double-shelled SnO_2 nano-polyhedra and their improved gas sensing properties. *Nanoscale* **2015**, *7*, 3276–3284.

200. Lou, Z.; Deng, J.; Wang, L.; Wang, L.; Fei, T.; Zhang, T., Toluene and ethanol sensing performances of pristine and PdO-decorated flower-like ZnO structures. *Sens. Actuators B Chem.* **2013**, *176*, 323–329.

201. Bing, Y.; Liu, C.; Qiao, L.; Zeng, Y.; Yu, S.; Liang, Z.; Liu, J.; Luo, J.; Zheng, W. Multistep synthesis of non-spherical SnO_2@SnO_2 yolk-shell cuboctahedra with nanoparticle-assembled porous structure for toluene detection. *Sens. Actuators B Chem.* **2016**, *231*, 365–375.

202. Dong, C.; Liu, X.; Xiao, X.; Du, S.; Wang, Y. Monodisperse $ZnFe_2O_4$ nanospheres synthesized by a nonaqueous route for a highly slective low-ppm-level toluene gas sensor. *Sens. Actuators B Chem.* **2017**, *239*, 1231–1236.

203. Iftekhar Uddin, A.S.M.; Chung, G.S. Effects of Ag nanoparticles decorated on ZnO nanorods under visible light illumination on flexible acetylene gas sensing properties. *J. Electroceram.* **2017**, *40*, 42–49.

204. Uddin, A.S.M.I.; Yaqoob, U.; Phan, D.T.; Chung, G.S. A novel flexible acetylene gas sensor based on PI/PTFE-supported Ag-loaded vertical ZnO nanorods array. *Sens. Actuators B Chem.* **2016**, *222*, 536–543.

205. Tamaekong, N.; Liewhiran, C.; Wisitsoraat, A, Phanichphant,S. Acetylene sensor based on Pt/ZnO thick films as prepared by flame spray pyrolysis. *Sens. Actuators B Chem.* **2011**, *152* 155-161.

206. Iftekhar Uddin, A.S.M.; Phan, D.T.; Chung, G.S. Low temperature acetylene gas sensor based on Ag nanoparticles-loaded ZnO-reduced graphene oxide hybrid. *Sens. Actuators B Chem.* **2015**, *207*, 362–369.

207. Zhou, Q.; Tang, C.; Zhu, S.P.; Chen, W.G.; Li, J. Synthesis, characterisation and sensing properties of Sm_2O_3 doped SnO_2 nanorods to C_2H_2 gas extracted from power transformer oil. *Mater. Technol.* **2016**, *31*, 364–370.

208. Zhang, H.; Chen, W.; Jin, L.; Cui, F. Hierarchically porous WO_3 microstructures with networks for acetylene sensing application. *Mater. Lett.* **2018**, *214*, 198–201.

209. Wang, B.; Jin, H.T.; Zheng, Z.Q.; Zhou, Y.H.; Gao, C. Low-temperature and highly sensitive C_2H_2 sensor based on Au decorated ZnO/In_2O_3 belt-tooth shape nano-heterostructures. *Sens. Actuators B Chem.* **2017**, *244*, 344–356.

210. Qiao, P.Y.; Zhang, L.X.; Zhu, M.Y.; Yin, Y.Y.; Zhao, Z.W.; Sun, H.N.; Dong, J.Y.; Bie, L.J. Acetylene sensing enhancement of mesoporous ZnO nanosheets with morphology and defect induced structural sensitization. *Sens. Actuators B Chem.* **2017**, *250*, 189–197.

211. Li, C.; Lin, Y.; Li, F.; Zhu, L.; Meng, F.; Sun, D.; Zhou, J.; Ruan, S. Synthesis and highly enhanced acetylene sensing properties of Au nanoparticle-decorated hexagonal ZnO nanorings. *RSC Adv.* **2015**, *5*, 87132–87138.

212. Chen, W.G.; Gao, T.Y.; Li, Q.Z.; Gan, H.I. Enhanced gas sensing properties of flower-like ZnO nanostructure to acetylene. *Mater. Technol.* **2014**, *30*, 96–100.

213. Shen, Z.; Zhang, X.; Ma, X.; Chen, Y.; Liu, M.; Chen, C.; Ruan, S. Synthesis of hierarchical 3D porous ZnO microspheres decorated by ultra-small Au nanoparticles and its highly enhanced acetylene gas sensing ability. *J. Alloys Compd.* **2018**, *731*, 1029–1036.

214. Lin, Y.; Li, C.; Wei, W.; Li, Y.; Wen, S.; Sun, D.; Chen, Y.; Ruan, S. A new type of acetylene gas sensor based on a hollow heterostructure. *RSC Adv.* **2015**, *5*, 61521–61527.

215. Iftekhar Uddin, A.S.M.; Lee, K.W.; Chung, G.S. Acetylene gas sensing properties of an Ag-loaded hierarchical ZnO nanostructure-decorated reduced graphene oxide hybrid. *Sens. Actuators B Chem.* **2015**, *216*, 33–40.